2017-10-14

INVESTIGATING EQUATORIAL ELECTROJET IRREGULARITIES USING COHERENT BACK SCATTER RADAR OVER BAHIR DAR REGION

HABTAMU, WUBIE

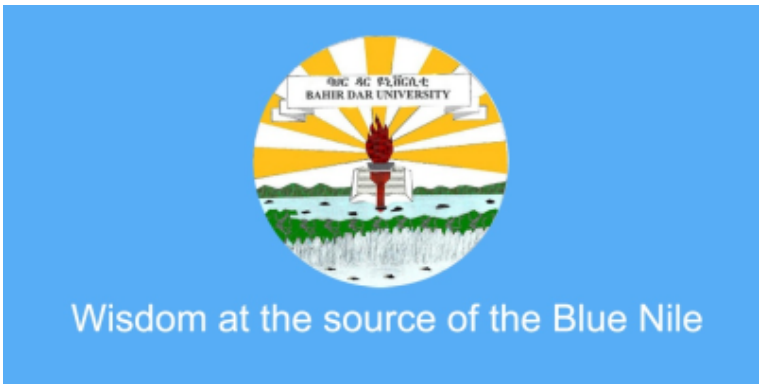

INVESTIGATING EQUATORIAL ELECTROJET IRREGULARITIES USING COHERENT BACK SCATTER RADAR OVER BAHIR DAR REGION

HABTAMU WUBIE

Bahir Dar

Bahir Dar University

June 8,2017

CERTIFICATION

The undersigned herby certify that they have read and recommend to the school of postgraduate studies for the acceptance of this project work entitled: "**INVESTIGATING EQUATORIAL ELECTROJET IRREGULARITIES USING COHERENT BACK SCATTER RADAR OVER BAHIR DAR** by **Habtamu Wubie** in Partial Fulfillment of the Requirements for the Degree of **MASTER OF SCIENCE IN PHYSICS** at Bahir Dar University..

APPROVED BY:

_____

Mellesew Nigussie(PhD), Supervisor

_____

_____

INVESTIGATING EQUATORIAL ELECTROJET IRREGULARITIES USING COHERENT BACK SCATTER RADAR OVER BAHIR DAR REGION

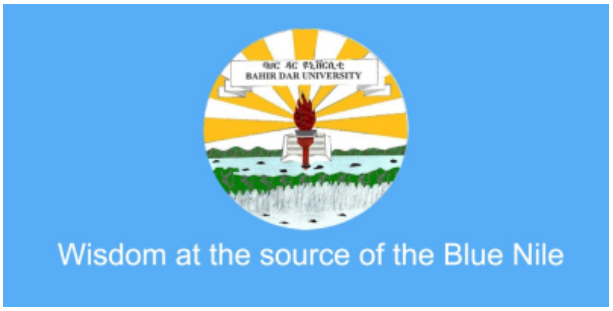

A Thesis Presented to
the School of Postgraduate Studies Bahir Dar University
in Partial Fulfillment of the Requirements for

the Degree of

MASTER OF SCIENCE IN PHYSICS

BY

HABTAMU WUBIE
June 8,2017

AUTHORIZATION TO COPY

Habtamu Wubie herby authorize the Bahir Dar University to copy and/or release the whole, part of this research work to other researchers and organizations wishing to use the material for reference and/or research purposes.

_____

ACKNOWLEDGEMENTS

First and for most I would like to thank GOD for his infinite mercy upon me. Then, I would like to thank deeply my supervisor Dr. Melessew Nigussie for his support throughout the duration of my thesis work. Though he is very busy of many works, he has been providing me encouragement, very deep and line by line comments and feedbacks. My thanks also goes to Mr Ambelu Tebabal for his unreserved and timely help and encouragement. This work will not be completed within the deadline without his great help. I want also to thank Fasil Tesemma for his kind response to any technical and scientific requests whenever I ask him. I would like to thank Head of physics department Dr. Tsegaye Kass for the courage he showed me when I was striving to complete the work in the given time. I would like to express my deep gratitude to Mr. Andarge Gerawork and his family for his long lasting support, encouragement and advice starting from my undergraduate education life. The encouragement and advice of my friends and colleagues, Meseret Lingerew, Dasash Mearegu and Selam Andualem is unforgettable and I would like to thank you deeply from my heart. The encouragement and continuous follow up of Derseh Yillie and Erkehun Zelalem was vital and and very important during this works and I would like to thank you deeply from my heart. Finally and most importantly I would like to thank my poor families who have been offering everything they have in my whole education life.

TABLE OF CONTENTS

List of Figures

Abstract

Equatorial ionospheric (e.g. equatorial electro-jet, EEJ) irregularity is a nuisance for technologies that depend on trans-ionospheric propagating radio waves. Significant efforts are being carried out to understand the EEJ irregularity; however, the African equatorial ionosphere that shows unique phenomena as observed by Low Earth Orbiting (LEO) satellite is the least investigated due to the lack of ionospheric monitoring instruments. In this thesis the spatial, temporal and statistical characteristics of equatorial electro-jet (EEJ) irregularities over Bahir Dar region are investigated using data from ground based Very High Frequency (VHF) Coherent Backscatter Radar, which is installed recently at Bahir Dar, Ethiopia and it is the first kind in Africa. One year data have been used and Doppler power spectral and statistical techniques have been applied to investigate the characteristics of the EEJ irregularity. It is found out that the EEJ irregularities were occurred, most frequently, between 99 and 102 km above sea-label within the time intervals of 10 to 14 LT (local time). Also, intense EEJ irregularities have been observed more frequently in the March equinox than other seasons. Moreover, the returned echoes of irregularities were found to have power spectra with peak power centered at zero or nearly zero Doppler shift. This indicates that the most dominant class of EEJ irregularity is type II. Some power spectra with mixture of type I and Type II were also observed in the returned echoes of the irregularities.

CHAPTER 1

INTRODUCTION

1.1 Background of the Study

The term ionosphere is applied to the upper part of the earth's atmosphere, extending upwards from about 55 to 1000 km, in which we find substantial numbers of free electrons and ions together with neutral atoms and molecules. The practical importance of the ionosphere lies in the communication field where it governs the propagation over long distances of radio waves of frequencies between about 10 kHz and 40 MHz (wavelengths 30 km and 7.5 m).

As atmospheric structures can nearly be organized by a representative temperature profile, ionospheric structures can also more sensibly be organized by electron number density profile . Basically, the attitudinal variation in the rate of production and rate of combination is the main reason to categorize the ionospheric structure into different regions,called D region, E region and F regions.

One of the most active regions of the earth's ionosphere is its equatorial ionospheric region where a number of phenomena are occurred under the influence of physical electrodynamics there. The horizontal orientation of magnetic field lines at the magnetic equator is the basic reason for the active nature of the lower latitudes of E and F regions of the earth's ionosphere even in the quit

geophysical conditions. Equatorial ionosphere exhibits some popular phenomenons like equatorial electrojet and the corresponding irregularities, post sunset enhancements in plasma drifts and equatorial spread F.

By the principle of dynamo effect the tidal winds in the equatorial E region of the ionosphere is the cause for the set up of an eastward strong primary electric field and hence an eastward electric current (Kelley, 1989). The combination of this primary eastward electric field with the horizontally oriented magnetic field at the dip equator gives rise to a vertical drift velocity for the plasma in the ionosphere. Since the upper and lower boundaries of the dynamo region are practically nonconducting, the Hall current is restricted,which leads to an enhanced eastward current flow,which is confined within 3^0 dip latitude, known as the equatorial electrojet, EEJ (Chapman, 1951). A strong equatorial electrojet occurs between 80 and 140 km in altitude (Kelley, 1989). This is because, in the range of this altitudes, conductivity of the plasma is maximum. In addition to this, at this height range, electrons are mainly controlled by the geomagnetic field rather than the collision with neutrals, where as the opposite is true for ions (Raghavarao & Dagar, 1982). The induced magnetic field of the equatorial electrojet is the cause for the daily variation of the earth's geomagnetic field strength at and near the magnetic dip equator (Cahil, 1959).

When an ionospheric plasma is forced to depart from its state of equilibrium by different geophysical and solar phenomena it is said to be in a state of instability. Depending on the available free energy in the plasma, various types of instabilities grow in the ionospheric plasma and these instabilities are responsible for the fluctuation of plasma densities and this is called ionospheric irregularities. The plasma density fluctuation in the EEJ is certainly associated with the instabili-

ties driven by strong EEJ current.

The modified two-stream instability and the gradient drift instability (GDI) are now believed to be responsible for the conventionally called type I and type II irregularities in EEJ, respectively. The two steam instability is excited when the the electron drift velocity with respect to the ions, exceeds the threshold value of ion-acoustic speed (Farley, 1963a) and the gradient drift instability (GDI) is created when the polarization electric field and the density gradient are in the same direction (Balsley, 1969). The gradient drift instability could coexist with the two stream instability at lower electron drift velocities.

Equatorial plasma irregularities have been extensively investigated using VHF coherent and incoherent scatter radars during the last few decades. In the American sector pioneering investigations have been carried out over JicamarcaPeru (Cohn, 1973) and investigations in Brazil were started recently over Sao Luios (Fejer & Kelley, 1980; Farley, 1985; Abdu *et al.*, 2002) VHF coherent back-scatter radars have been used to study the equatorial electrojet irregularities, also at other longitude sectors, notably, in India (Muralikrishna, 1976; Patra, 2005) and in Africa (Carter *et al.*, 1976).

The common outcomes of these investigations are that the E region around the center of EEJ is the seat for both of these two types of instabilities as the conditions for the GDI and two stream instabilities to occur are satisfied. Type I echoes have been observed under strongly driven conditions (strong EEJ current) due to the corresponding drift velocity of electrons exceed the threshold value. The favorable condition for the existence of type II radar echoes is found to be the same polarity of the vertical polarization electric field with the vertical electron density gradient in the

E region. Type II radar echoes were also observed at low altitude more frequently than type I radar echoes.

1.2 Statement of the problem

Ionospheric irregularities generally, and equatorial electrojet irregularities specifically, are the main causes for the scintillation of radio signals traversing the equatorial region of the earth's ionosphere. Ionospheric scintillation of radio signals has a significant impact on communication , navigation and positioning operations of ground and space born devices. Since ionospheric scintillation originates from random electron density irregularities acting as wave scatterers, research on the formation and evolution of ionospheric irregularities is vital.

Equatorial electrojet irregularities in other longitudinal sectors have been studied using HF and VHF coherent back scatter radar systems both at and nearby the magnetic equator. A few investigations have been also done regarding to EEJ's temporal characteristics (Mangistu & Kassa, 2015) and also its effect on equatorial ionospheric irregularity over East African sector (Seba & Nigussie, 2016) using magnetometer data. In general, the African equatorial ionosphere that shows unique phenomena as observed by Low Earth Orbiting (LEO) satellite is the least investigated ionospheric region due to the lack of ionospheric monitoring instruments (Hei *et al.*, 2005). Studying EEJ irregularities using coherent back scatter radar systems is more preferable than using magnetometers. This is because, while magnetometer data enable us to investigate temporal variation of EEJ, coherent backscatter radar systems enables us to study both the spatial and

temporal variation of EEJ and its irregularities. The Blue Nile coherent Backscatter radar system which is installed in Bahir Dar, Ethiopia, is one of those recently installed VHF radar systems. The system could help us to characterize the EEJ irregularities, i.e., to determine the most probable height and local time for the occurrence of EEJ irregularities which can't be determined using only magnetometer. In addition to this, we can also investigate the dominant driving force for the excitement of the EEJ irregularities in our equatorial electrojet sector.

1.3 Objectives

General Objectives

The generalized aims of this work are:

- To characterize equatorial electrojet irregularities.

Specific Objectives

The specific tasks of this work are:

- To determine the most probable height and local times for the occurrence of the EEJ irregularities.
- To investigate the seasonal variation of the intensity of equatorial electrojet irregularities.
- To determine the dominant type of EEJ irregularities over Bahir Dar region.

1.4 Significance of the study

This study will show the extent to which the observed EEJ irregularities will occur both spatially and temporally. The study will indirectly try to show how much is the impact of the observed irregularities on the performance of navigation,positioning and terrestrial communication systems. The work will also concentrate to indicate when (in terms of local time) and where (in terms of altitude) an intensified EEJ irregularities and, therefore, an intense radio wave distortion and degradation of the communication systems could be occurred. This will have its own input for those who will design and operate several communication, navigation and positioning systems in the region where this work is conducted.

CHAPTER 2

Earth's Equatorial Ionosphere

2.1 Introduction

The ionosphere is a partially ionized gas consisting of thermally free electrons and ions in the upper region of the atmosphere that envelops the Earth's atmosphere and space. The free electrons and ions are produced via ionization of the neutral particles both by extreme ultraviolet radiation from the Sun, which is called photo-ionization, and by collisions with energetic particles, which is normally known as impact ionization, that penetrate the atmosphere. The ionosphere does not entirely disappear at night because the necessary recombination time for the ions and electrons (the average time required for all the ions and electrons to unite to form neutral particles) is long enough for the layer to persist overnight. The recombination rate is determined by background density and is consequently high at low altitudes (where density is high), and decreasing with altitude as the density falls. The degree of ionization at any given point is a balance between the rate of production of ions (photoionization), and the rate of loss of ions (recombination). Once formed, the charged particles are affected by a set of processes, including chemical reactions, diffusion, wave disturbances, plasma instabilities, and transport due to electric and magnetic fields. This chapter highlight the constituent and altitudes of parts of ionosphere, discuss basics of equa-

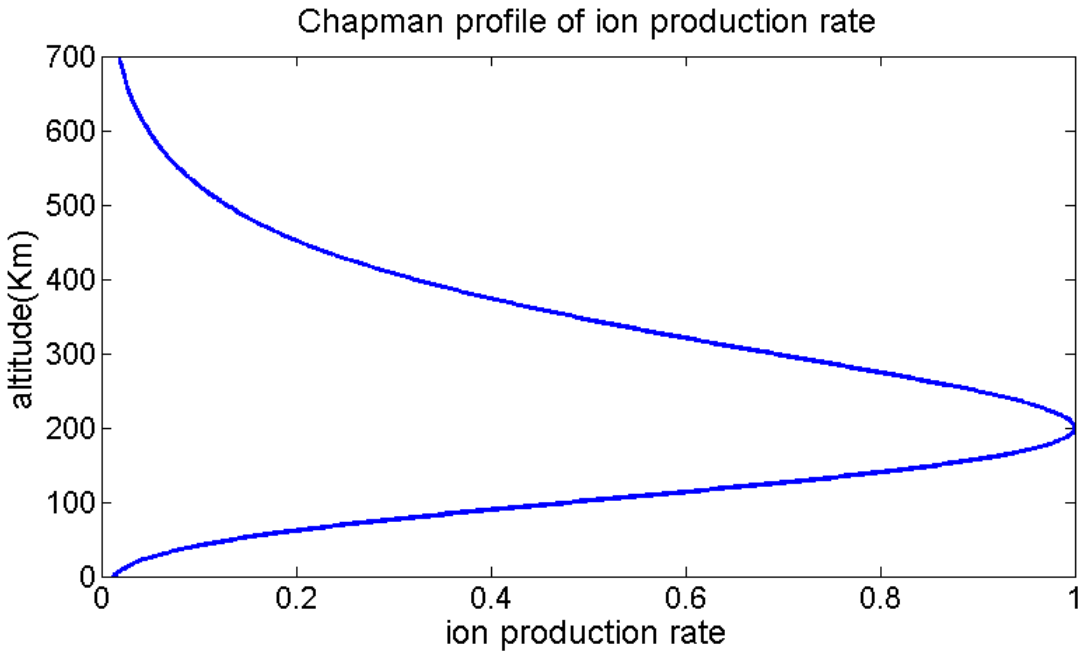

Figure 2.1: Generalized vertical structure of ionosphere

torial ionospheric electrodynamics and the known ionospheric conductivities. More importantly, in this chapter more emphasis is given to discussing basics principles of equatorial electrojet generations and its characteristics. Then, finally the chapter is concluded by presenting detail derivations of instabilities and characterizing the resulting irregularities.

2.1.1 Parts of Ionosphere

The earth's ionosphere begins at an altitude of about 60 km and extends beyond 1000 km, with the peak electron concentration occurring at approximately 300 km. Based on the altitude variation in the rate of production and rate of combination the ionospheric structure is divided into different regions,called D region, E region and F region. The lowermost part of the ionized atmo-

sphere covering the altitude range of 60 - 90 Km is called D region ionosphere. Ionization in this region is mainly produced from nitric oxides by the Lyman α - line and from oxygen molecules by EUV or X-rays. The altitude range of 90 - 150 km of the ionosphere is called E region of the atmosphere. During the day time the E region has an electron density profile with typical electron concentrations of around $10^{11}/m^3$. Since there are very few direct mechanisms (there is no direct incoming solar radiation) of ion and electron production during night time, the electron density drops to around $10^9/m^3$ at night. Maximum electron density in the E region generally occurs near $\approx 100km$. Ionization in this region arises due to the absorption of EUV between 80 nm and 102.6 nm and X-rays from 1 nm to 10 nm. The most abundant ions in this region are found to be oxygen ion and nitrogen oxide ion.

On the other hand the altitude range above 150 Km is called F region. The equatorial F region has a peak electron concentration of $10^{12}/m^3$ during the day, which drops by an order of magnitude at night. The altitude of peak ionization generally lies in the range of 200 - 400 Km. The most abundant ions in this region are oxygen. ionOften during day time, F region is divided into F_1 and F_2 basically because of the altitude variation of rate of production and loss of ionization.

The altitude profile of plasma density in the ionosphere is very complicated which depends on the three processes of production, loss(recombination) and transport. The incoming solar radiation is the main source of ionization energy. Similarly, the neutral atoms and molecules in the atmosphere are also another main sources for the ionized particles in the ionosphere. Roughly speaking,therefore, the rate of production of ionized particles is directly proportional to the product of the coming radiation intensity (I) and the neutral number density (n), which decreases

exponentially with altitude. The solar radiation has the highest intensity when it is outside the atmosphere. When the radiation penetrates into the atmosphere,the rate of production increases due to increasing n. But, when the number density is increased further the absorption of radiation by the overlaying atmosphere may become appreciable and I starts to decrease. Thus,the rate of production, being proportional to the product of n and I, must therefore exhibit a peak. The resulting altitude profile of plasma density in the ionosphere is called Chapman profile which is depicted in the Figure 2.1. The Chapman profile in Fig (2.1) shows clearly that the electron number density initially increases with altitude and attains a maximum and starts to decrease continuously.

2.2 Equatorial Ionosphere

Once routine monitoring of the ionosphere had become widespread, it soon became known that certain aspects of the behavior of the equatorial ionosphere differed greatly from the behavior of the ionosphere elsewhere. It was found that these differences were not determined by the geographic equator, but were related to the dip equator. The location of the dip (or magnetic) equator is usually described as the locus of points of zero magnetic field dip angle along the surface of the Earth. Magnetic dip angle is the angle made with the horizontal by the Earth's magnetic field line. The dip equator and geographic equator coincide at only two points-in the mid-Pacific and mid-Atlantic oceans. From Central Africa to India the dip equator closely follows the 10^0 N. parallel but in South America it reaches as far south as 15^0.

Due to the unique configuration of mutually perpendicular electric field (east-west), magnetic field (north-south) and electron density gradient (upward), the equatorial ionosphere is the active ionospheric region where most important electrodynamical phenomena such as Equatorial ElectroJet (EEJ), Counter Equatorial ElectroJet (CEEJ), Equatorial Ionization Anomaly (EIA), Equatorial Spread-F (ESF) and Midnight Temperature Maximum (MTM), are usual to exist there.

2.2.1 Basics of Equatorial Ionospheric Plasma Dynamics

The ions, electrons, and neutrals in the ionospheric plasma can be considered as three interpenetrating fluids coupled by collisional and electromagnetism forces and also in addition individually they are subjected to gravitation and pressure gradient forces. The ionospheric plasma fluid is governed fundamentally by the continuity equation, the momentum equation and the ideal gas equation of state.

While the the continuous ionization and recombination of ions and electrons leads to temporal variation of electron number densities, the transportation of the plasma as whole leads to spatial variation of electron densities in the ionosphere. The continuity equation relates the temporal and spacial variation of charged particle number densities (n_j) with the rate of production (P_j) and loss (L_j) of charged particles in the ionosphere.

$$\frac{\partial n_j}{\partial t} + \nabla \cdot (n_j \, V_j) = P_j - L_j \tag{2.1}$$

where V_j is the velocity of each charged species. The production term is determined by the density and properties of the neutral molecules as well as the ionizing radiation and the detailed ionization process. The loss rate depends on the electron/ ion densities and the rate coefficients

of the recombination process.

Assuming the constituents of the ionospheric plasma behaves as an ideal gas,the particle number density (n_j) and pressure(P_j) for each species are related by the ideal equation of state as.

$$P_j = n_j \, kT_j \tag{2.2}$$

The equation of motion for an ionized particle is given by

$$M_j \, n_j \frac{DV_j}{Dt} = -\nabla P_j + M_j \, n_j \, \mathbf{g} + n_j \, q_j \, (\mathbf{E} + \mathbf{V_j} \times \mathbf{B}) - M_j \, n_j \, \nu_j (\mathbf{V_j} - \mathbf{u}) \tag{2.3}$$

where $D = \frac{\partial}{\partial t} + (\mathbf{V_j} \cdot \nabla)\mathbf{V_j}$ is called the material derivative. ν_j is the collision frequency of either the ions or electrons with neutral particles and u is velocity of neutral particles.

The first term in right hand side of equation (2.3) is the pressure gradient force,the second term is gravitational force while the third one is Lorentz force and finally the fourth term is the collision force. From equation (2.3) we can notice that the acceleration term is in the order of $\mathbf{V_j}/\tau + \mathbf{V_j^2}/L$ where τ and L are time and distance scales over which velocity change is significant, the Lorentz force is in the order of $\mathbf{V_j}\Omega_j$, where $\Omega_j = q_j \, B/M_j$ is the gyro frequency of ions and electrons about the geomagnetic field and the collision force is in the order of $\mathbf{V_j}\nu_j$. Practically the gyro frequency and collision frequencies are very large numbers. Thus, for $\tau \gg \Omega^{-1}, \nu^{-1}$,the left hand side of (2.3) will vanish immediately. In addition, for a horizontally stratified ionospheric plasma, the gravitational force should be balanced by the pressure gradient force. Finally,the equation of steady state ionospheric plasma motion for ions and electrons becomes;

$$0 = ne \, (\mathbf{E} + \mathbf{V_i} \times \mathbf{B}) - m_i \, n \, \nu_i (\mathbf{V_i} - \mathbf{u}) \tag{2.4}$$

$$0 = -ne(\mathbf{E} + \mathbf{V_e} \times \mathbf{B}) - m_e \, n \, \nu_e (\mathbf{V_e} - \mathbf{u}) \tag{2.5}$$

After some mathematical manipulations and rearrangements, the velocity of electrons and ions are obtained to be

$$\mathbf{V_e} = -e\mathbf{k_e} \cdot \mathbf{E} \tag{2.6}$$

Here electron mobility,$\mathbf{k_e}$ is given by

$$\mathbf{k_e} = \begin{pmatrix} k_{ep} & k_{eH} & 0 \\ -k_{eH} & k_{ep} & 0 \\ 0 & 0 & k_{e\parallel} \end{pmatrix} \tag{2.7}$$

Where each elements of $\mathbf{k_e}$ are called Pederson mobility (k_{eP}),Hall mobility(k_{eH}) and the parallel mobility ($k_{e\parallel}$) and they are mathematically given by

$$k_{ep} = \frac{1}{eB}\frac{\Omega_e \nu_e}{\Omega_e^2 + \nu_e^2} \tag{2.8}$$

$$k_{eH} = \frac{1}{eB}\frac{\Omega_e^2}{\Omega_e^2 + \nu_e^2} \tag{2.9}$$

$$k_{e\parallel} = \frac{1}{m_e \nu_e} \tag{2.10}$$

Similar expressions for ion velocity and mobility is also obtained.

$$\mathbf{V_i} = e\mathbf{k_i} \cdot \mathbf{E} \tag{2.11}$$

where each element of the ion mobility has the same definition to that of electrons and their expression is given by

$$k_{ip} = \frac{1}{eB}\frac{\Omega_i \nu_i}{\Omega_i^2 + \nu_i^2} \tag{2.12}$$

$$k_{iH} = \frac{1}{eB}\frac{\Omega_i^2}{\Omega_i^2 + \nu_i^2} \tag{2.13}$$

$$k_{i\parallel} = \frac{1}{m_i \nu_i} \tag{2.14}$$

Combining the charge continuity equation (neglecting the effect of ion production and loss), $\mathbf{J} = ne(\mathbf{V_i} - \mathbf{V_e})$, with that of Ohms law,$\mathbf{J} = \sigma \cdot \mathbf{E}$, one could obtain the following well known equation,

$$\sigma = ne^2(\mathbf{k_i} + \mathbf{k_e}) \tag{2.15}$$

Inserting the expressions of $\mathbf{k_i}$ and $\mathbf{k_e}$ into equation (2.15) will give the known expression of conductivity as

$$\sigma = \begin{pmatrix} \sigma_p & \sigma_H & 0 \\ -\sigma_H & \sigma_p & 0 \\ 0 & 0 & \sigma_\parallel \end{pmatrix} \tag{2.16}$$

Each components of the conductivity tensor in equation (2.16) can be defined in the following way.

Parallel conductivity(σ_0):It is responsible for the flow of current parallel to the geomagnetic field. Mathematically, it is given by:

$$\sigma_0 = N\, e^2 \left(\frac{1}{m_e\, \nu_e} + \frac{1}{m_i\, \nu_i} \right)$$

It is independent of strength of the geomagnetic field and is much larger than Pedersen and Hall conductivities in the ionosphere.

Pedersen conductivity(σ_p): It is the cause for the flow of current along the perpendicular (to the geomagnetic field) component of the electric field ($\mathbf{E}_\perp$).

$$\sigma_p = N\, e^2 \left(\frac{\nu_e}{m_e(\nu_e^2 + \Omega_e^2)} + \frac{\nu_i}{m_i(\nu_i^2 + \Omega_i^2)} \right)$$

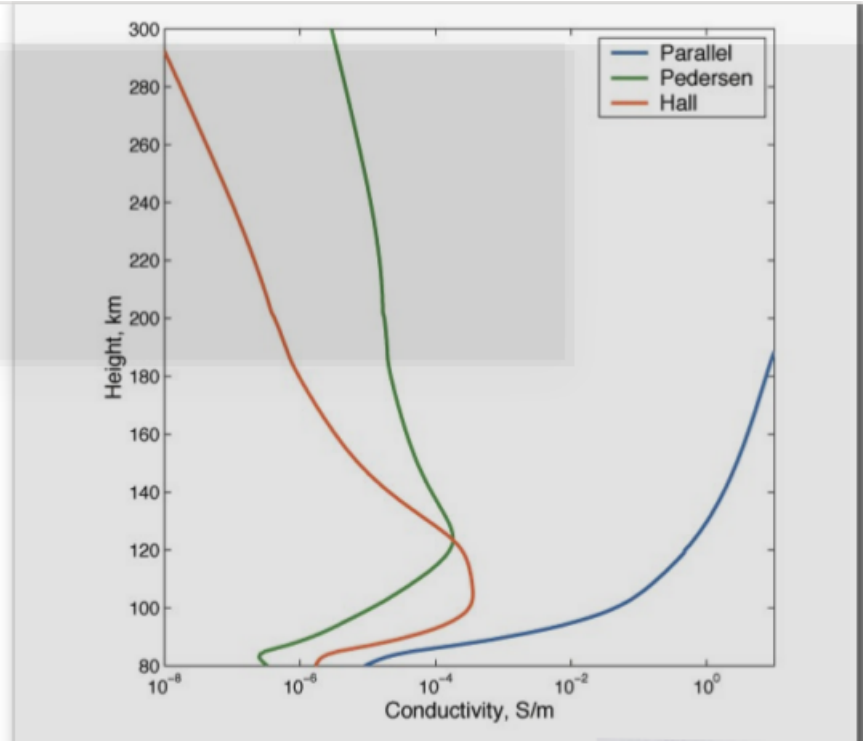

Figure 2.2: Altitude variation of ionospheric conductivities (adopted from M.Nigussie, 2014)

Hall conductivity(σ_H): It is responsible for the drift of electrons and ions in a direction perpendicular to both $\mathbf{E}$ and $\mathbf{B}$.

$$\sigma_H = N\, e^2 \left(\frac{\Omega_e}{m_e(\nu_e^2 + \Omega_e^2)} + \frac{\Omega_i}{m_i(\nu_i^2 + \Omega_i^2)} \right)$$

Figure (2.2) shows some typical curves to indicate the variation of the three conductivities ($\sigma_\parallel, \sigma_P$ and σ_H) with altitude. Except for the lowest part of the ionosphere, the parallel (to the magnetic field) conductivity is much higher than the perpendicular components. Thus, the electric field component along the magnetic field,$\mathbf{E}_\parallel$, will generally be less than the perpendicular component,$\mathbf{E}_\perp$

2.3 The Equatorial Electrojet

The earth's ionosphere acts not only as the reflector or absorbent layer of the radio wave but also as layer of electric current. The driving forces of ionospheric currents are tidal forces in the earth's atmosphere produced by the sun and the moon and the uneven heating of earth's atmosphere by sun. These two forces results in a horizontal charged particles motions across earth's magnetic field which in-turn induces an electromotive force (electric field).

The combination of Lorentz and Coulomb forces drives electric currents at altitudes in the ionosphere where the air is electrically conducting, causing daily variations in the geomagnetic field. The entire process is called atmospheric dynamo theory. An ionospheric plasma subjected to electric ($\mathbf{E}$) and magnetic ($\mathbf{B}$, with unit vector $\hat{\mathbf{b}}$) fields produces an ionospheric current whose corresponding current density is given by

$$\mathbf{j} = \sigma_0 \, \mathbf{E}_{\parallel} + \sigma_p \, \mathbf{E}_{\perp} - \sigma_H \, \left(\mathbf{E} \times \hat{\mathbf{b}} \right) \tag{2.17}$$

Since the Coriolis force vanishes at the equator and the gravitational force is negligible at higher altitudes, the only force that could drive the neutral equatorial atmosphere is the pressure gradient force, $-\nabla P$ (Nigussie, 2014). This force comes from the differential solar heating of the earth's atmosphere. In the day side of the equatorial atmosphere, the wind should blows in the direction of $-\nabla P$ from east to west across the sunset terminator. On the other hand, at the E region altitudes the electron gyrofrequency exceeds the electron - neutral collision frequency while ion - neutral collision frequency exceeds ion gyro frequency i.e., $\Omega_e > \nu_e$ and $\nu_i > \Omega_i$ (Raghavarao & Dagar, 1982). Figure (2.3) shows the altitude variation of electrons and ions collision frequen-

cies together with their gyrofrequencies. The figure clearly indicates that the electrons' collision frequencies is much less than its gyrofrequencies but the opposite is true for ions. Consequently, the ions are carried across the magnetic field with the wind but the electrons carried across the wind gyrating about the geomagnetic field lines. The relative movement of the electrons and ions constitute charge separation which in turn produces an east - west horizontal electric field.

Consider a coordinate system where x points towards east,y points vertically downward and z points into the plane of this page as shown in Fig (2.4).

Initially, the eastward electric field, which is developed by the dynamo action of the horizontal wind, in combination with northward geomagnetic field produces current according to equation (2.17). Specifically, in this scenario we have a horizontal electric field, $\mathbf{E} = E_x\ \hat{i}$ and as a result $\mathbf{E}_{\parallel} = 0, \quad \mathbf{E}_{\perp} = E_x\ \hat{i}$ and $\mathbf{E} \times \hat{\mathbf{b}} = -E_x\ \hat{j}$. Substitute this to equation (2.17) and obtain,

$$j_{1x} = \sigma_p\ E_x \tag{2.18}$$

$$j_{1y} = \sigma_H\ E_x \tag{2.19}$$

This result is depicted in Fig (2.4a). The vertical Hall current, $j_y = \sigma_H\, E_x$, is however inhibited by a horizontally stratified ionosphere bounded by a collisionless plasma from the above (and hence the ions and electrons drift to the same direction with the same speed results in null current) and by the neutral atmosphere (insulator to electric current) from the bottom side of the dynamo region (80 - 140 km). Extreme case of inhibition to vertical ionospheric current occurs at the dip equator (Raghavarao & Dagar, 1982).

The inhibition of vertical current gives rise to accumulation of charges at the top and bottom parts

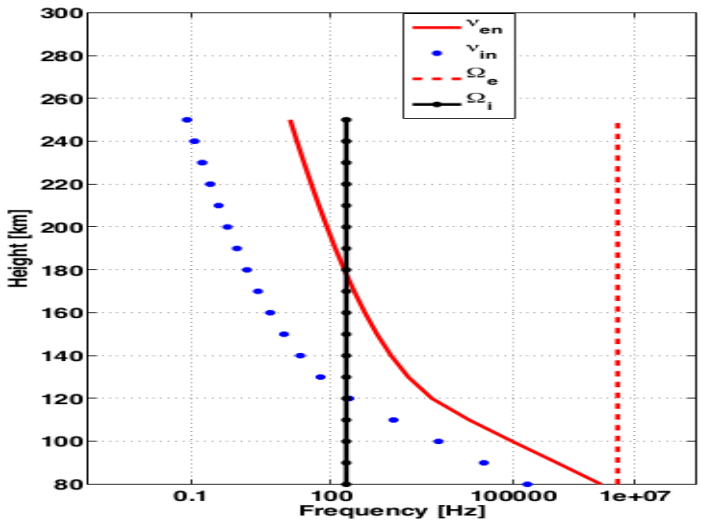

Figure 2.3: Altitude variation of ion and electron collision frequencies with neutrals (adopted from M.Nigussie, 2014)

of the dynamo region and this in turn enables development of vertical polarization electric field, $\mathbf{E} = -E_y\hat{j}$. In this scenario we have,$\mathbf{E} = -E_y\hat{j}$. The required components in this scenario become,$\mathbf{E}_{\parallel} = 0$, $\mathbf{E}_{\perp} = -E_y\ \hat{j}$ and $\mathbf{E} \times \hat{\mathbf{b}} = -E_y\ \hat{i}$. By the same procedure, the current density produced by this vertical polarization electric field and the geomagnetic field using equation(2.17) becomes

$$j_{2x} = \sigma_H\ E_y \tag{2.20}$$

$$j_{2y} = -\sigma_p\ E_y \tag{2.21}$$

This result is shown diagrammatically in Fig (2.4 b). The negative sign in (2.21) is to show that j_y points vertically upwards based on the given coordinate system. Inhibition of vertical current at the magnetic equator makes the resultant vertical current to be vanished. Thus, equations (2.19)

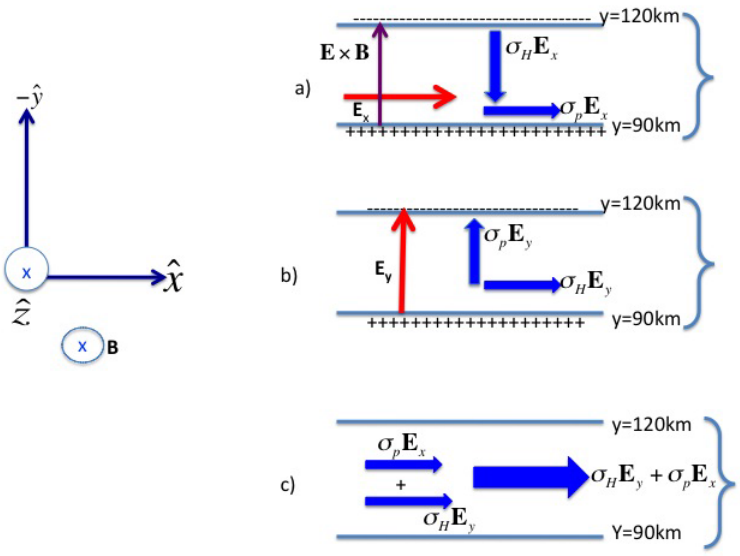

Figure 2.4: Mechanism equatorial EEJ formation,adopted from M.Nigussie (adopted from M.Nigussie, 2014)

and (2.21) are combined to give

$$E_y = \frac{\sigma_H}{\sigma_p} E_x \tag{2.22}$$

The resultant horizontal (eastward) current is obtained by combining equations (2.18),(2.20) and (2.22). This yields

$$J_x = \left(\sigma_p + \frac{\sigma_H^2}{\sigma_p}\right) E_x \tag{2.23}$$

The corresponding conductivity for the eastward current density which is called Cowling conductivity is then becomes

$$\sigma_c = \frac{J_x}{E_x} = \sigma_p + \frac{\sigma_H^2}{\sigma_p}$$

The flow of the resultant horizontal current is also shown clearly in Fig (2.4 c).

Thus, the enhanced conductivity in the eastward direction gives rise to enhanced eastward electric current. Chapman (1951) named this east - west enhanced ionospheric current in the vicinity of the dip equator as **equatorial electrojet (EEJ)**. The latitudinal extent of EEJ is about $\pm 3^0$ about the dip magnetic equator. The equatorial electrojet corresponds to an east-west electric field of 0.5 mV/m and a vertical polarization field of about 10 - 15 mV/m. This gives rise to an eastward current or westward electron drift of several hundred m/s. The electron drift is westward by day and eastward at night. Studies conducted by Burrows (1970) near Peruvian have indicated that there is longitudinal variation of electron drift velocities which is may be due to longitudinal altering of local dip angles.

The equatorial electrojet is confined in the altitude of the order of 90 km to perhaps 140 km (Farley, 1963b). The altitude profile of each components of the ionospheric conductivity is the main determining factor for the vertical position of the EEJ. The reason why it is confined only to this altitude range (90 km to perhaps 140 km) is associated with the conductivity of the region. At lower altitudes the conductivity of the ionosphere is very low because of the high frequency collision resulting from greater neutral particle density. On the other hand at higher altitudes the Cowling conductivity is very low because of the lower ion and electron gyro frequencies. The decreasing of ion and electron gyro frequencies at higher altitudes is because of the decreasing of the strength of earth's magnetic field at higher altitude. The height profile of the ratio of (σ_H/σ_P), which is the dominant term in the Cowling conductivity, is drawn and presented in (Fig 2.5). From the figure we can notice that the ratio is maximum around 100 km in the E region of the ionosphere. The extremely large conductivity ratio is the cause for strong vertical

polarization field and hence a strong horizontal electric current due to $\mathbf{E} \times \mathbf{B}$ drift which is called EEJ. In addition, from Fig.(2.2) we can see that as the altitude increases between 80 and 140 km, σ_p increases so that E_y decrease, which is actually the deriving force of EEJ, with height thus limiting the altitude extent of the electrojet. Generally, when the collision frequencies of both the ions and electrons are smaller than their respective gyro frequencies, the crossed electric and magnetic fields enforce the ions and electrons to drift together with the velocity $\frac{\mathbf{E}\times\mathbf{B}}{B^2}$ and as a result there will not be any net current. But fortunately, in the conducting region the ratio of collision frequency to gyrofrequency is generally less than 1 for the electrons but greater than 1 for the ions.

The large quit day daily variation of the horizontal magnetic field strength, H, around the dip

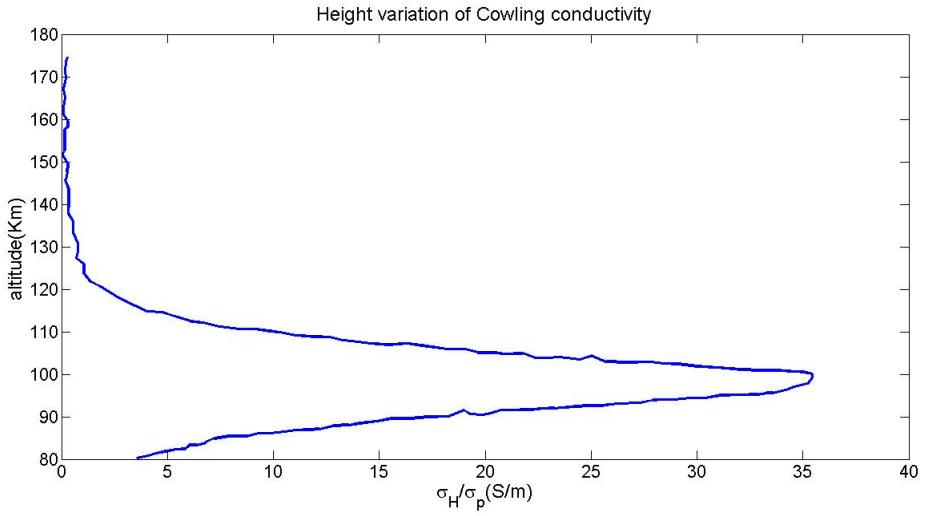

Figure 2.5: The ratio (σ_H/σ_P) as a function of height

equator has been attributed to the equatorial electrojet (Chapman, 1951). It has been found that (Osborne, 1963) the electrojet contribution to the horizontal variation of the earth's magnetic field

falls within about 6^0 latitude of the magnetic equator. There is large daily variation in intensity, position (in terms of altitude) and width of equatorial electrojet. It is also reported that the peak value of ΔH, which is the proxy of strength of EEJ, occurred at a latitude significantly displaced from the magnetic equator. Studies conducted to investigate seasonal variability of the strength of EEJ have shown that the EEJ us more intense during equinoctial periods than at other times of the year (Burrows, 1970). The day to day variability of the lunar and solar tides, which are primary sources of the meridian electric field,is responsible for the day to day variability of the strength of EEJ (Osborne, 1963). These variations, as pointed out by the previous researchers, are caused by the strong influence of tidal modes which in turn have strong seasonal dependence.

2.4 Equatorial Electrojet Irregularities

The ionosphere can be considered as a continuous layer of charged particles with a fairly smooth plasma density distribution. However,when the ionosphere is perturbed, localized structuring of plasma can occur,leading to the development of ionospheric electron density irregularities. The equatorial and low latitude ionospheric region is the most active and common candidate region of many irregularity triggering electrodynamic phenomenas. Since, external disturbing agents are not often required for the development of ionospheric irregularities in this region, the occurrence of irregularities even on geomagnetically quiet periods is one of the distinctive attributes of the equatorial ionosphere. Equatorial electrojet irregularity which is associated with irregular distribution of plasma density in the zonal region of EEJ is one of the commonly observed irregularity

in the equatorial ionosphere.

Ionospheric irregularities are produced when ionospheric plasma instabilities induced by available free energies are excited in the ionosphere. Plasma instabilities in the EEJ are driven either by the streaming electrons in the EEJ which is called two-stream instability or by the electron density gradient there which is called gradient drift instability. Specifically, therefore, the equatorial electrojet irregularity is induced by the different classes of instabilities which are excited in and by EEJ itself.

Usually space plasma are subjected to Lorentz force, Coulomb's force, pressure gradient forces and the drag forces (due to collisions of neutrals with ions and electrons). The governing equations for the ionospheric plasma in the EEJ, are the continuity equations and the momentum equations. For a single ion species and electrons, the continuity equations for electrons and ions in the unperturbed state are given by

$$\frac{\partial n_0}{\partial t} + \nabla \cdot [n_0 \mathbf{V_{e0}}] = 0 \tag{2.24}$$

$$\frac{\partial n_0}{\partial t} + \nabla \cdot [n_0 \mathbf{V_{i0}}] = 0 \tag{2.25}$$

and the steady state equations of motion under the unperturbed conditions are also given as

$$0 = -e\, n_0 \,[\mathbf{E_0} + \mathbf{V_{e0}} \times \mathbf{B}] - \nabla P_0 - m_e\, \nu_e\, n_0\, \mathbf{V_{eo}} \tag{2.26}$$

$$0 = e\, n_0\, [\mathbf{E_0} + \mathbf{V_{i0}} \times \mathbf{B}] - \nabla P_0 - m_e\, \nu_i\, n_0\, \mathbf{V_{io}} \tag{2.27}$$

while in the perturbed state, the continuity and the momentum equations for both ions and electrons becomes

$$\frac{\partial}{\partial t}\left(n_0+n\right)+\nabla\cdot\left[(n+n_0)(\mathbf{V_{e0}}+\mathbf{V_e})\right] = 0 \tag{2.28}$$

$$\frac{\partial}{\partial t}\left(n_0+n\right)+\nabla\cdot\left[(n+n_0)(\mathbf{V_{i0}}+\mathbf{V_i})\right] = 0 \tag{2.29}$$

and

$$\begin{aligned} m_e\left(n_0+n\right)\frac{D}{Dt}(\mathbf{V_{e0}}+\mathbf{V_e}) &= -e\left(n_0+n\right)\left[\mathbf{E_0}+\mathbf{E}+(\mathbf{V_{e0}}+\mathbf{V_e})\times\mathbf{B}\right]-\nabla\left(P+P_0\right) \\ &\quad -m\nu_e\left(n_0+n\right)\left(\mathbf{V_{eo}}+\mathbf{V_e}\right) \end{aligned} \tag{2.30}$$

$$\begin{aligned} m_i\left(n_0+n\right)\frac{D}{Dt}(\mathbf{V_{i0}}+\mathbf{V_i}) &= e\left(n_0+n\right)\left[\mathbf{E_0}+\mathbf{E}+(\mathbf{V_{i0}}+\mathbf{V_i})\times\mathbf{B}\right]-\nabla\left(P+P_0\right) \\ &\quad -m\nu_e\left(n_0+n\right)\left(\mathbf{V_{io}}+\mathbf{V_i}\right) \end{aligned} \tag{2.31}$$

where ionospheric parameters with subscript *'0'* represents the values before perturbations, while those without this subscript represent the values added due to perturbations.

We supposed that the geomagnetic field $\mathbf{B}$ is unperturbed by the presence of the plasma and is known. Similarly, the collision frequencies of ions with neutrals and electrons with neutrals (ν_i, ν_e), which primarily depend on the neutral density, are also supposed known. The plasma is assumed to be quasi-neutral; i.e., the electron and ion densities are approximately equal before and after perturbations ($n_{0i} \approx n_{0e} = n_0$ and $n_i \approx n_e = n$). The ionization-recombination terms which should appear on the right-hand sides of continuity equations have been omitted as well.

This is because typical ionization-recombination times are of the order of several hours, which is about the typical growth time of the instability. Therefore, these terms would make only a small correction to the analysis below and have been omitted for the sake of simplicity.

Subtract equations (2.24) from (2.28), (2.25) from (2.29), (2.26) from (2.30) and (2.27) from (2.31) to obtain the following set of equations.

$$\frac{\partial n}{\partial t} + \nabla \cdot [n(\mathbf{V_{e0}} + \mathbf{V_e}) + n_0 \, \mathbf{V_e}] = 0 \tag{2.32}$$

$$\frac{\partial n}{\partial t} + \nabla \cdot [n(\mathbf{V_{i0}} + \mathbf{V_i}) + n_0 \, \mathbf{V_i}] = 0 \tag{2.33}$$

and

$$m_e \frac{D}{Dt}(\mathbf{V_{e0}} + \mathbf{V_e}) = -e\,[\mathbf{E} + \mathbf{V_e} \times \mathbf{B}] - \frac{\nabla P}{n + n_0} + \frac{n \nabla P_0}{n_0(n + n_0)} - m_e \, \nu_e \, n \, \mathbf{V_e} \tag{2.34}$$

$$m_i \frac{D}{Dt}(\mathbf{V_{i0}} + \mathbf{V_i}) = e\,[\mathbf{E} + \mathbf{V_i} \times \mathbf{B}] - \frac{\nabla P}{n + n_0} + \frac{n \nabla P_0}{n_0(n + n_0)} - m_i \, \nu_i \, n \, \mathbf{V_i} \tag{2.35}$$

The above set of equations can be simplified by taking further assumptions. The ions,before perturbation are considered to be stationary ($\mathbf{V_{io}} = \mathbf{0}$) and unmagnetized (their gyrofrequenies is much less than their collision frequencies,i.e., $\Omega_i \ll \nu_i$) Ω_i) at EEJ heights. Compared to ions, electrons have negligible inertia this makes the left hand side of equation (2.34) to be zero. Taking the plasma as an ideal gas of temperature T, the pressure is given by $P = nKT, P_0 = n_0 \; KT$. Since $n \ll n_0$ for small perturbations, the third term on the right hand side of equations (2.34) and (2.35) can be neglected. The electric field wave is essentially assumed to be electrostatic

(as it should be for the assumed time invariant geomagnetic field) ,i.e, it can be derived from scalar potential ϕ using $\mathbf{E} = -\nabla\phi$. Inserting these assumptions and mathematical expressions into equations (2.34) and (2.35) gives,

$$0 = -\frac{e}{m_e}\left[-\nabla\phi + \mathbf{V_e} \times \mathbf{B}\right] - u_e^2 \frac{\nabla n}{n_0} - \nu_e \mathbf{V_e} \tag{2.36}$$

$$\left(\frac{\partial}{\partial t} + \mathbf{V_i} \cdot \nabla\right)\mathbf{V_i} = -\frac{e}{m_e}\nabla\phi - u_i^2 \frac{\nabla n}{n_0} - \nu_i \mathbf{V_i} \tag{2.37}$$

where $u_e^2 = \frac{kT}{m_e}$ and $u_i^2 = \frac{kT}{m_i}$ are the thermal velocities of electrons and ions respectively. The continuity equations in (2.32) and (2.33) can also be simplified further by imposing the above assumptions together with the fact that the product of two first order perturbations is very small and can be neglected in the expansion of these equations. The imposed assumptions and restrictions on to equations (2.32) and (2.33) results in

$$\frac{\partial n}{\partial t} + \nabla \cdot [n\mathbf{V_{e0}} + n_0 \mathbf{V_e}] = 0 \tag{2.38}$$

$$\frac{\partial n}{\partial t} + \nabla \cdot [n_0 \mathbf{V_i}] = 0 \tag{2.39}$$

We chose a Cartesian coordinate system in which the x axis is aligned with earth's magnetic field (north), the y direction is west and the z direction is vertically upward.

If we now assume perturbations to be horizontally traveling waves of the form $exp\, i(ky - \omega t)$, as usual we can substitute the spatial operator ∇ and temporal operator $\frac{\partial}{\partial t}$ by $i\ k\ \hat{j}$ and $-i\ \omega$ respectively into equations equations (2.36) through (2.38). This modifies equations (2.36) and

(2.38) into;

$$i(k\,V_d - \omega)n + V_{ez}\frac{\partial n_0}{\partial z} + i\,kn_0\,V_{ey} = 0 \tag{2.40}$$

$$\nu_e\,V_{ey} + \Omega_e\,V_{ez} = i\,k\left(\frac{e\phi}{m_e} - u_e^2\,\frac{n}{n_0}\right) \tag{2.41}$$

$$\nu_e\,V_{ez} - \Omega_e\,V_{ey} = 0 \tag{2.42}$$

where, $V_d = V_{0ey}$ is the drift velocity of the electrons relative to the ions. The second term of the distributed right hand side of equation (2.38) is second order and as a result it can be neglected for very small perturbations. Similarly, applying the linear wave analysis to equations (2.37) and (2.39) will yields,

$$-i\,\omega\,n + i\,k\,n_0\,V_{iy} = 0 \tag{2.43}$$

$$(\nu_i - i\omega)V_{iy} = -i\,k\left(\frac{e\phi}{m_i} + u_i^2\,\frac{n}{n_0}\right) \tag{2.44}$$

Equations (2.40) through (2.44) forms five systems of linear equations with five unknowns. The system of equations is solved to obtain

$$\omega - k\,V_d = \frac{\psi}{\nu_i}\left[\omega(i\omega - \nu_i) - ik^2\,C_s^2\right]\left(1 - \frac{i\Omega_e}{\nu_e\,k\,L}\right) \tag{2.45}$$

where $C_s^2 = \left(\frac{m_e}{m_i}\right)\,u_e^2 + u_i^2$ is the ion acoustic velocity,

$$\psi = \frac{\nu_e\,\nu_i}{\Omega_e\,\Omega_i}$$

and

$$L = n_0\,\left(dn/dz\right)^{-1}$$

is the density gradient scale length.

Equation (2.45) is called the dispersion equation relating the propagating vector k to its frequency of oscillation ω. Decompose ω into its real and imaginary parts,that is:

$$\omega = \omega_k + i\,\gamma_k \tag{2.46}$$

with both ω_k and γ_k are both real numbers. Thus, the irregularity we considered above has two components; the oscillatory term, $exp\ i(ky - \omega_k t)$ and the the instability exciting term, $exp\ (-\gamma_k t)$. In order to determine the very minimum required value for the excitation of instability, we have to impose a restricting condition where,

$$|\gamma_k| \ll |\omega_k|$$

and then substituting (2.46) into (2.45) and considering the restricting condition given above, we obtained;

$$\omega_k = \frac{k\,V_d}{1+\psi} \tag{2.47}$$

and

$$\gamma_k = \frac{\psi}{1+\psi}\left\{\frac{\Omega_e}{\nu_e}\,\frac{\omega_k}{kL} + \left(\omega_k^2 - k\,C_s^2\right)\frac{1}{\nu_i}\right\} \tag{2.48}$$

When the density gradient is ignored (i.e.$L \longrightarrow \infty$)that means the spatial distribution of electron number density is is assumed to be uniform, we can obtain the two stream instability growth condition by setting the instability growth term to be positive,i.e. by setting $\gamma_k > 0$ in equation (2.48) the two stream instability growth condition becomes,

$$V_d > C_s\,(1+\psi) \tag{2.49}$$

where $\mathbf{V_d}$ is the zero-order westward (daytime) electron drift velocity.

The root physical mechanism by which the two stream instability arises can be explained in brief as follow. A plasma consisting of two or more inter-penetrating streams of charged particles will be unstable (longitudinal waves will grow spontaneously) if the mean velocity of the particles in one stream is sufficiently great relative to the mean velocity of the particles in the other. Particles traveling at velocities close to the phase velocity of the wave interact with the wave. If more particles are decelerated by the wave than are accelerated, the wave gains energy and grows. Equation (2.49) suggests that in regions where strong ionospheric currents (large value of V_d) are dominant, plane acoustic waves will indeed appear spontaneously.

If we take $\nu_e \approx 4 \times 10^4 \ s^{-1}, \nu_{\approx} 2.5 \times 10^3 \ s^{-1}, \Omega_e \approx 5 \times 10^6 \ s^{-1}, \Omega_i \approx 90 \ s^{-1}, C_s^2 = 10^5 \ m^2/s^2, L = 6 \times 10^3 \ m$ at the most probable height of EEJ , $105 \ km$,the minimum electron drift velocity required for the generation of two stream instability using equation (2.49) becomes $350 \ m/s$ (Farley, 1973).

At long wavelengths (small k), the gradient term becomes more and more important and the gradient drift instability growth condition is similarly obtained by imposing $\gamma_k > 0$ into equation (2.48). Thus, when the following condition is satisfied, gradient drift instability will be developed.

$$\frac{\nu_i}{1+\psi}\frac{\Omega_e}{\nu_e}\frac{V_d}{L} > k^2\left[C_s^2 - V_d^2\left(1+\psi\right)^{-2}\right] \tag{2.50}$$

Note that L is positive for density increasing with altitude and V_d is positive for electrons drifting toward the west, the usual daytime conditions.

Similarly, if we substitute the values given above into equation (2.51) we find the wavelength

$(\lambda = 2\pi/k)$ of the unstable wave using (2.51) to be roughly

$$\lambda \geq \frac{300}{\sqrt{V_d}} \tag{2.51}$$

The minimum wave length of the unstable wave excited by gradient drift instability is then becomes

$$\lambda_c = \frac{300}{\sqrt{V_d}} \tag{2.52}$$

Equation (2.53) indicates that irregularities with wavelength $100\ m$ or more can be generated by almost any magnitude of drift velocity with proper sign. But according to this equation irregularities with wavelength in the order of meter or short wavelength cannot be excited by drift velocities less than the ion acoustic velocity, C_s.

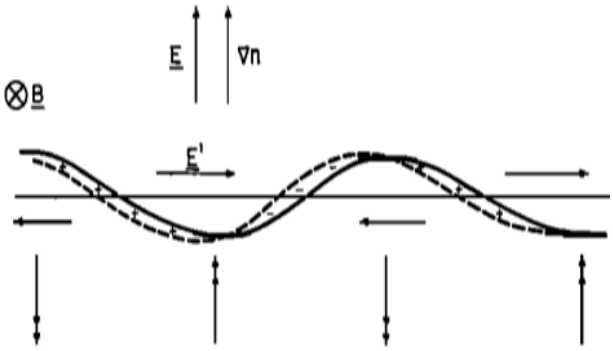

Figure 2.6: Simplified physical picture of gradient drift instability

Gradient drift instability in EEJ is driven by the electric potential ϕ_0 energy as the gravitational fluid instability is driven by gravitational potential energy in fluid dynamics. EEJ instability arises whenever the electron density increases in the same direction the electron potential energy, $-e\phi$,

increases. The basic physical mechanism is explained by taking a very simplified picture of space plasma neglecting the effect of gravitational force there as shown in Fig. (2.6). The horizontal line represents an unperturbed contour of constant electron concentration, the steady density gradient and electric field are both directed upward; the magnetic-field vector is directed into the plane of paper. If now the density is perturbed by a small-amplitude sinusoidal variation, the $\mathbf{E} \times \mathbf{B}$ drifts of the ions and electrons will carry them both to the left. Since the Hall mobility of the ions is always less than that of the electrons, space charges will appear, giving rise to small-scale electric fields $\mathbf{E}'$ directed alternately to left and right. The corresponding $\mathbf{E}' \times \mathbf{B}$ drifts will then carry the enhanced regions downward and the depleted regions upward, so that they will both appear to grow in amplitude against the background density. Obviously, if either the electric field or the steady density gradient were reversed in direction, the perturbations would tend to disappear, and we would have a stable situation.

Throughout the above derivations, we have confined to a limiting condition where the developed irregularity is assumed to have a wave vector (direction of propagation) in the direction of electron drift velocities and as a result the two stream instability growth condition given in equation (2.49) is restricted to an irregularity wave propagating only in the direction of electron drift velocities. To accompany all possible direction of irregularity wave propagation, equation (1.47) should be generalized to an arbitrary wave direction $\mathbf{k}$ and could be written as

$$\omega_k = \frac{\mathbf{k} \cdot \mathbf{V_d}}{1 + \psi} \tag{2.53}$$

where $\mathbf{V_d}$ is the zero-order electron drift velocity.

2.4.1 Characteristics of Equatorial Electrojet Irregularities

The presence of equatorial electrojet irregularities have been verified from the backscattered VHF radar signals and scintillated VHF radio waves traversing the EEJ region. The linear kinetic treatment of instabilities together with early experimental work revealed that the strong current in the electrojet region was undoubtedly responsible in some way for the production of the irregularities that caused the radar echoes(Farley, 1973). The experimental observation has also indicated that the power of the radar signal backscattered from the volume of electrojet region directly above the magnetic equator increased sharply when the magnetic field induced by the EEJ current exceeds some critical value (Cohen & Bowles, 1963). It has been further demonstrated by Cohen & Bowles (1963) that the strength of the echoes received from these irregularities is closely related, and sometimes proportional, to the current density in the electrojet.

In the day time side of equatorial electrojet sector, electrons are known to drift horizontally towards the west (Balsely, 1973). Since, the electron drift velocity is horizontal, the corresponding irregularity traveling horizontally in the direction of the electron motion will be the most strongly excited wave and should give the strongest radar signal echoes. The irregularities in EEJ are field aligned irregularities where the geomagnetic field lines are parallel to the wave front of the irregularity and perpendicular to the direction of propagation of the irregularities (Cohen & Bowles, 1963; Balsely, 1973).

As we discussed above,the modified two-stream instability and the gradient drift instability (GDI) are now believed to be responsible for the conventionally called Types I and II irregularities in EEJ, respectively (Balsley, 1969; Farley, 1963b).

Type I irregularity arises only when the electron drift velocity V_d, constituting the Hall current in the EEJ, exceeds roughly the ion acoustic velocity,C_s, which is roughly 350m/s. Radar echoes from type I Irregularities are strong and have a narrow Doppler spectrum which is sharply peaked at a phase velocity comparable to or somewhat greater than the ion-acoustic velocity. Usually, phase velocity of type I remains the same in all direction in the magnetic east west plane (Cohen & Bowles, 1963). More importantly, the position of the peak in the power spectra of type I irregularities was constant when the zenith angle was between 45^0 and 70^0 both to the east and to the west (Cohen & Bowles, 1967) . This is clearly shown in Fig (2.7) which consists of series of spectra taken from the equatorial electrojet irregularities at different elevation angles obtained at Jicamarca during a period of relatively strong scattering (Cohen & Bowles, 1967). As shown in the figure the peak of the power spectrum obtained from a vertical radar is centered at zero Doppler shift. The spectra are normalized to the peak value. The basic reason that the phase velocity of type I irregularities is independent of zenith angle of the radar (but the zenith angle should be between 45^0 and 70^0) is that in a scattering volume bounded by these angles (45^0 and 70^0), there is some region where the total vector drift velocity (zero order plus perturbation drift) in the direction of the radar exceeds the two stream threshold (Kelley *et al.*, 2008). According to the linear kinetic theories of two stream instability, the phase velocity of type I irregularities is comparable to the ion acoustic velocity in the electrojet region for electron drift velocities just above threshold value (Farley, 1963b) and this was verified by experimental observations conducted previously. The study (Cohen & Bowles, 1967; Balsely & Farley, 1971) found that the electron drift velocity can exceed threshold value but the phase velocity of the resulting type I ir-

regularities remains the constant which shows its independence with the electron drift velocities. When the electric field remains less than the threshold required for the two-stream wave generation, the dominant instability processes is that of the gradient drift mode (GD) that produces the Type-2 irregularities. Type II irregularities are triggered when the polarity of electron density gradient is the same as that of the polarization electric field, whose magnitude should also be greater than some threshold value ($E \geq 3\ mV/m$) (Raghavarao, 2002). This is actually a day time phenomenon of bottom side of E region where the electron density gradient, Δn, is parallel to the polarization electric field, both pointing vertically upward. Type II irregularities are characterized by weaker radar echoes and a broader Doppler spectrum with a peak in the vicinity of zero or nearly zero Doppler shift. The average phase velocity of the type 2 irregularities is smaller than the ion acoustic velocity and is approximately proportional to the cosine of the radar elevation angle (Balsley, 1969). Balsley (1969) has verified this by an experiment conducted at the Jicamarca radio observatory using 49.92 MHz VHF radar. In his experiment Balsley (1969) has probed the EEJ irregularities nearly at the same time by using an oblique and vertical radars. The power spectra of the returned echo for each case (for vertical and oblique radar) is shown in Fig (2.8). From the figure it is clearly seen that when the radar's line of sight is vertical the peak of the power spectrum occurs at zero Doppler shift and when the radar's line of sight is tilted either towards the west or east the power spectrum attains its peak to greater Doppler shift.

An important characteristic of the type II irregularities is that they tend to move with a mean velocity roughly identical with that of electrons' drift velocities (Balsley, 1969). That means, type-2

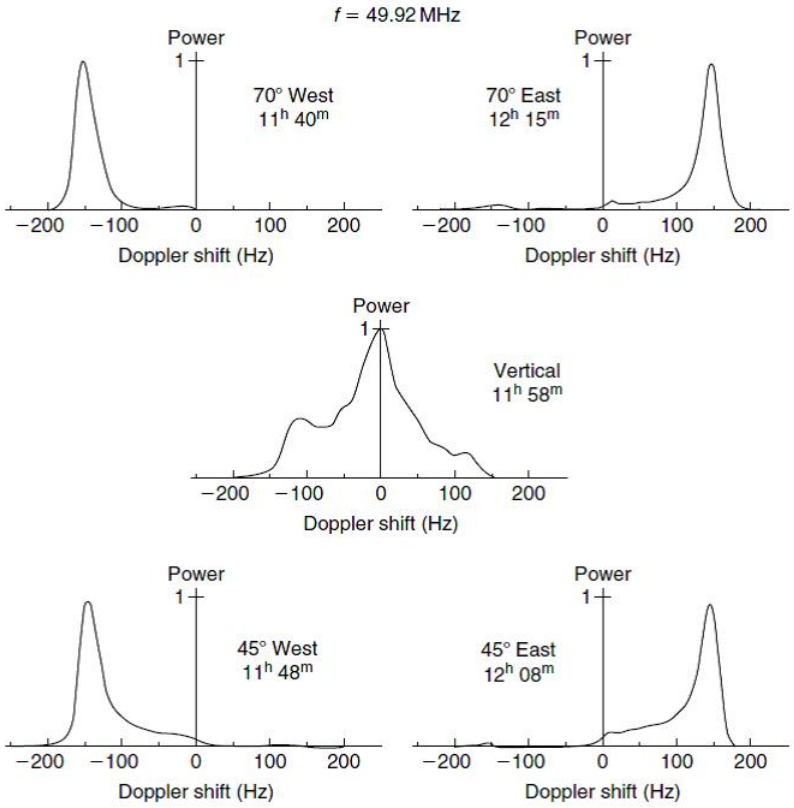

Figure 2.7: Series of Doppler spectra from the equatorial electrojet irregularities. [Cohen and Bowles (1967)].

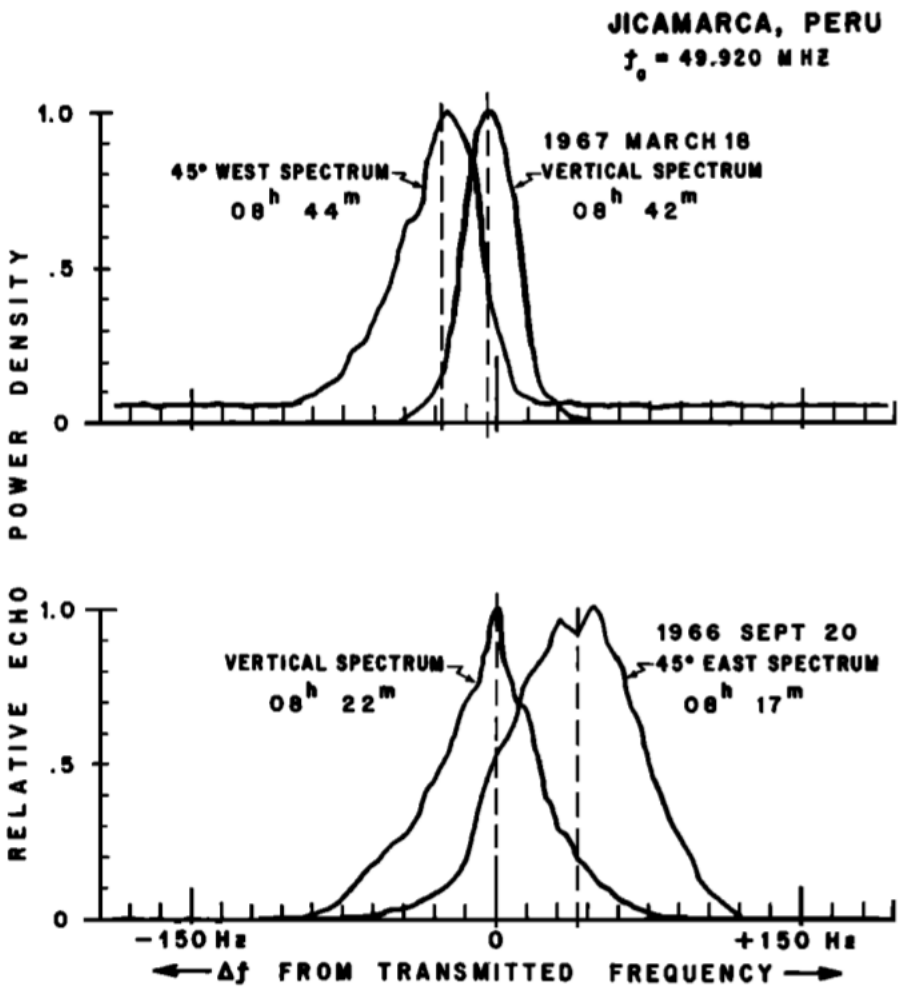

Figure 2.8: Vertical and oblique spectra comparing vertical and horizontal motions of the type II irregularities[Balsely (1969)]

spectra is a measure of the plasma drift velocity V_d, , and hence the vertical or zonal electric field, as indicated by the expressions given in Equation (2.22). Experimental observations (Balsley, 1969) indicated that the strength of scattered signal from type II irregularities was proportional to the square of electron drift velocities,at least for velocities no exceeding ion acoustic velocity. Generally, type II irregularities are observed when the electrojet current density is low, give rise to Doppler shifts smaller than those predicted by two stream theory and often exhibits a clear bifurcation of the echoing region when the electrojet intensity is well below its normal midday value.

EEJ irregularities whose observed characteristics couldn't be described by the linear theory of two stream instabilities and gradient drift instabilities (which are discussed in detail above) were found using coherent backscatter radars. Previous studies (Balsley, 1969) have identified small scale (short wavelength in the order of $3m$) irregularities for electron drift velocities less than the ion - acoustic velocity. Such class of irregularities cannot be attributed neither to linear theory of two stream instability (which requires electron drift velocity greater than ion - acoustic velocity to induce irregularity)nor to linear theory of gradient drift instability (which produce irregularities with wavelength in the order of several tens of meters or longer). None linear gradient instability theory (which is not discussed here in this work), which involves nonlinear coupling process was developed to address such classes of instabilities and found to be in agreement with experiment (Sudan *et al.*, 1973). According to the theory, type II irregularities with a wavelength of 3 meters are observed even when the mean electron drift velocity is quite small.

2.5 Measurement Techniques Of Ionospheric Irregularities

The ionosphere is a remarkable medium for electromagnetic wave propagation. Since the beginning of the radio age, study has been conducted to determine the structure of ionosphere and the spatial and temporal variation of its state variables like temperature, electron number density, ionospheric currents. Its effect on the radio communication and navigation systems which is generally called ionospheric scintillation has been also studied in detail using different instruments like ionosondes, in situ satellite measurements and ground based magnetometers.

Since then, considerable effort and resources were consequently devoted to investigating efficient (in terms of resources and functioning) instruments that could enable us to probe the parts of the ionosphere where the previous instruments were unable to observe and analyze.

2.5.1 Basics of Radar systems

A radar is an electrical system that transmits radio frequency (RF) electromagnetic (EM) waves toward a region of interest and receives and detects these EM waves when reflected from objects in that region. The captured signal is used to calculate the distance from the target to the radar and/or the velocity of moving the target.

A radar system commonly consists a transmitter,antenna, receiver, and signal processor. The subsystem that generates powerful pulses and/or waveforms of electromagnetic energy at precise time intervals and sends them to the antenna block is the transmitter. The antenna is the subsystem that takes as input these EM waves from the transmitter and introduces them into the propagation medium (normally the atmosphere). It also picks up the returning echo energy and

passes it to the receiver with minimal loss of energy. The T/R device has the function of providing a connection point so that the transmitter and the receiver can both be attached to the antenna simultaneously and at the same time provide isolation between the transmitter and receiver to protect the sensitive receiver components from the high powered transmit signal.

The transmitted signal propagates through the environment to the target. The EM wave induces currents on the target, which re-radiates these currents into the environment. In addition to the desired target, other surfaces on the ground and in the atmosphere re-radiate the signal. These unintentional and unwanted but legitimate signals are called clutter. Some of the re-radiated signal radiates toward the radar receiver antenna to be captured. The radar receiver antenna receives the target reflected energy from the antenna block. It then performs amplification, filtering, demodulation and applying analog-to-digital conversion on the received signal. The preprocessed signal is then sent to a computer or signal processor for further processing. The detector is the device that removes the carrier from the modulated target return signal so that target data can be sorted and analyzed by the signal processor.

The range, R, to a detected target can be determined based on the time,Δt , it takes the EM waves to propagate to that target and back at the speed of light. It is given by

$$R = \frac{c\Delta t}{2} \tag{2.54}$$

Range ambiguity occurs when continuous pulse streams are sent and continuous echoes from the targets are received by the radar. Since all the pulses are identical, the radar cannot identify which echo originated from which pulse, and this gives rise to an ambiguity in the range measurement. For a radar system with pulse repetition interval, T,the maximum unambiguous detection range

can be computed as follows:

$$R_{max} = \frac{cT}{2}$$

Range resolution is the ability of a radar system to distinguish between two or more targets at different ranges. The minimum distance required between two targets to be resolved by a radar system of pulse width τ is given by

$$\Delta R = \frac{c\tau}{2}$$

There are two basic antenna configurations of radar systems: monostatic and bistatic. In the monostatic configuration, one antenna serves both the transmitter and receiver. In the bistatic configuration, there are separate antennas for the transmit and receive radar functions.

2.5.1.1 Coherent and Incoherent radar systems

Radar systems can be configured to be incoherent or coherent. A radar is said to be coherent, if it stores in its memory a record of the phases and amplitudes of all transmitted pulses. The phase of any two transmitted pulses from coherent radars is consistent; i.e., there is a continuity in the signal phase from one pulse to the next. A pulsed coherent system measures the phase of the received signal on a pulse-to- pulse basis. This reference sinusoid is usually implemented in the form of a local oscillator (LO) signal used to produce the transmit signal that also serves as the reference for the received signal. If the local oscillator signal is a fixed frequency, it can serve as a reference for measuring the phase of the received signal. Since Doppler represents a frequency shift in the received signal, only coherent radars can extract Doppler information. This is because

the instantaneous frequency of a signal is proportional to the time derivative of the signal phase. Coherent scatter radars can work at modest power levels and with relatively compact antennas. On the other hand an incoherent radar system detects only the amplitude of the received signal. The amplitude of the signal at any instant in time will determine the brightness of the corresponding area of the display face. However, incoherent scatter radars (ISRs) are powerful, large, expensive facilities requiring considerable resources to install, operate and maintain.

2.5.1.2 Ionospheric Coherent Back-scatter Radar

While Incoherent scatter involves a weak radio scattering from thermal fluctuations in the ionospheric plasma, coherent scatter, in general, means scattering that is stronger than incoherent scatter but weaker than total reflection. The detection of coherent radar scatter generally implies the existence non-thermal irregularities in the plasma, indicative of free energy, waves, and instabilities.

Coherent scatter commonly occur in the ionospheric E region, where tow stream and gradient drift instabilities produce intense field aligned plasma irregularities (FAIs). Because of the high mobility of electrons along the direction of geomagnetic field, the density irregularities are field aligned. There are at least two parameters to be determined by coherent back scatter type of radar that are important for the purpose of the study of ionospheric plasma. The first and the most common one is the intensity of the backscatter signal when it is sorted into range and time bins (range- time-intensity format). The phase velocity of the irregularities and correspondingly

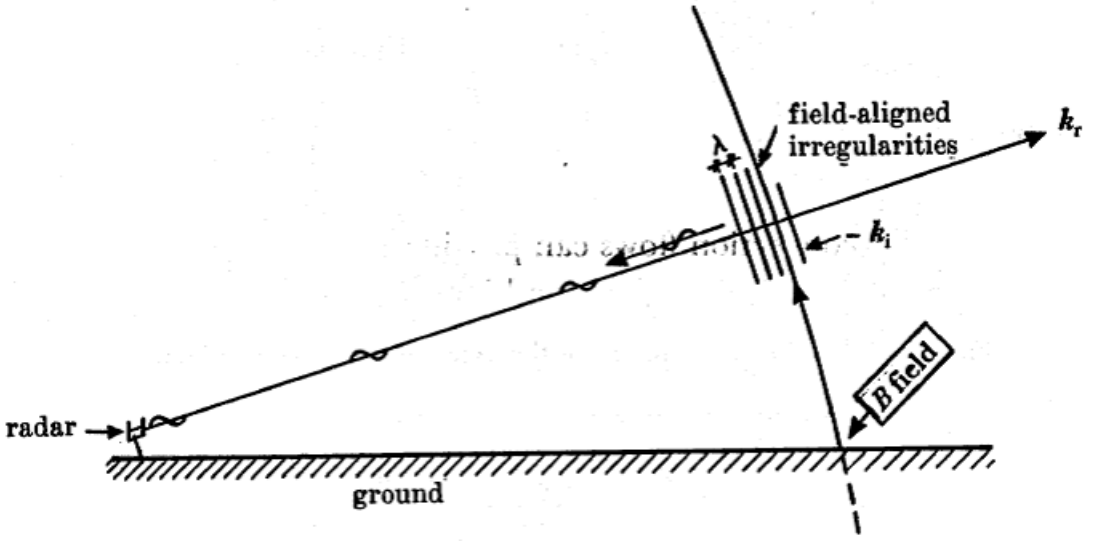

Figure 2.9: Schematic diagram of radar beam showing orthogonality to field-aligned irregularities and geometry of coherent radar observations.

the drift velocity of electrons can be determined from the Doppler power spectrum graphs. The class of the observed irregularity can also be determined based on the determined magnitude of phase velocity of the irregularity.

Probing field aligned irregularities with a proper angle of elevation by coherent radar is required to produce coherent back-scatter. To produce coherent back-scatter, the separation of field aligned irregularities (localized density structures) along the radar beam field must be equal to half of the radar wavelength and the radio wave from the radar should incident perpendicular to the plane of field aligned irregularity waves or alternatively to the geomagnetic field (Bragg's condition). This requirement is depicted exactly in Fig (2.9). Thus, the relation between the wave vector of the transmitted radar signal ($\mathbf{k_t}$) and that of the the irregularity wave ($\mathbf{k_i}$) are related by

$$\mathbf{k_i} = -\mathbf{2k_t} \tag{2.55}$$

Substitute equation (2.55) into equation (2.53) and use $\mathbf{V_p} = \omega_\mathbf{k}/\mathbf{k_i}$ to obtain a mathematical expression for the phase velocity (V_p) of the irregularity towards or away from the radar along the radar's line of sight. This yields in

$$V_p = \frac{-\mathbf{2k_t} \cdot \mathbf{V_d}}{1 + \psi} \tag{2.56}$$

where $\mathbf{V_d}$ is the zero-order electron drift velocity.

2.5.1.3 Doppler Effect and Frequency shift

For stationary target, the frequency or wavelength generated by the wave source (transmitter) will be the same at the receiver site; that is $f_r = f_s$,where the subscripts r and s refer to wave receiver and wave source, respectively. If there is relative motion between the radar and the target, then the frequency of the EM wave reflected from the target and received by the radar will be different from the frequency of the wave transmitted from the radar. This frequency difference or shift is called the Doppler frequency. The Doppler frequency shift,f_d,is the difference between the frequency of the received wave and that of the transmitted wave and is approximately given by

$$f_d = \frac{2v_r}{\lambda} \tag{2.57}$$

where v_r is the radial component of the target's velocity vector and λ is the wavelength of the transmitted EM wave. It can also be written as

$$f_d = \frac{2V\cos\theta}{\lambda} \tag{2.58}$$

where θ is the angle between the radar's line of sight (pointing away from the radar's receiver) and the velocity vector,$\mathbf{V}$ of the object. If the target moves towards the receiver, f_d will be negative

and vice-verse.

Noise, Signal-to-Noise ratio, and Detection

Because of random thermal motion of charged particles, all objects in the universe with a temperature above absolute zero will be radiating EM waves at, collectively, almost all frequencies. These EM waves, called thermal noise, are always present at the radar's receiving antenna and compete with the reflected EM waves from the target. In addition, the radar's receiver, being an electrical device with randomly moving electrons, generates its own internal thermal noise that also competes with the received target signal.

If the signal power of the reflected EM wave from the target is much greater than the noise power due to environmental and receiver noise, the presence of a target echo signal can be revealed by setting an amplitude threshold above the noise level (but below the target level). Any received signals (plus noise) that are above this amplitude threshold are assumed to be returns from targets, while signals below this threshold are ignored. This is the basic concept of threshold detection. To increase the probability of detection, the target signal power must be increased relative to the noise power. The ratio of the target signal power to noise power is referred to as the signal-to-noise ratio.

2.5.2 Basics of Digital Signal Processing

2.5.2.1 Sampling

The Nyquist sampling theorem states that, the digital signal will adequately represent the original analog signal if the samples are taken at a rate greater than twice the highest frequency in the analog signal. Let the maximum frequency component of $x(t)$ be f_m, then to recover the signal $x(t)$ exactly from its samples it has to be sampled at a rate $f_s \geq 2f_m$. While the continuous (analog) signal is represented by $x(t)$, the sampled signal is represented by $x[n]$. The digital signal $x[n]$ is obtained by evaluating $x(t)$ at $t = n/f_s$ for $n = 0, 2, 3, \cdots$.

If the initial samples are not sufficiently closely spaced to represent high-frequency components present in the underlying function, then the DFT values will be corrupted by aliasing. This in turn makes it impossible to reconstruct the original signal from its samples. As before, the solution is either to increase the sampling rate (if possible) or to pre-filter the signal in order to remove its high-frequency spectral content. It follows, therefore, that anti-aliasing filters are essentially analog filters that restrict the maximum frequency component of the input signal to be less than half of the sampling rate.

2.5.2.2 Data collection

Consider a pulsed radar, for each pulse transmitted a series of complex samples of the echo corresponding to successive range intervals will be collected at the out put of the receiver. By the Nyquist criterion, these range samples are collected at a rate equal to or greater than the pulse width. Range samples are defined as range gates or bins. This process is repeated a number of

times for each of pulses transmitted in the coherent processing interval.

2.5.2.3 Convolution

Convolution is a mathematical computation that measures the effect of a system on a signal. It is a mathematical tool used to compute the out put,$y[n]$, of a system whose impulse response is $h[n]$ and excitation signal (input signal) is $x[n]$. Mathematically it is given by

$$y[n] = \sum_{-\infty}^{\infty} h[k]\, x[n-k] \tag{2.59}$$

The impulse response,$h[n]$, of a system is the series of output samples it would generate over time if a unit impulse signal (an instantaneous pulse of infinitesimally small duration which is zero for all subsequent sampling instants) were to be fed as its input.

2.5.3 Fourier Analysis

2.5.3.1 The Discrete Fourier Transform

Fourier analysis is instrumental to radar signal processing, both for detection and Doppler shift evaluation.

The Discrete Fourier Transform (DFT) is the equivalent of the continuous Fourier Transform for signals known only at N instants separated by sample times $T_s = 1/f_s$ (i.e. a finite sequence of data). Let $x(t)$ be be the continuous signal which is the source of the data. Let N samples be denoted $x[0], x[1], x[2], \cdots, x[N-1]$. The Fourier transform of the original signal, $x(t)$, would

be

$$X(j\omega) = \int_{-\infty}^{\infty} x(t)\, e^{-j\omega t} dt \tag{2.60}$$

Then, since the integrand exists only at the sample points: The integral in equation (3.7) becomes,

$$X(j\omega) = \sum_{k=0}^{N-1} x(k)\, e^{-j\omega kt} \tag{2.61}$$

We could in principle evaluate this for any ω, but with only N data points to start with, only N final outputs will be significant. Since the operation treats the data as if it were periodic, we evaluate the DFT for the fundamental frequencies and for its harmonics($\omega = 0$). That is, evaluate the DFT equation at

$$\omega = 0,\ \ \frac{2\pi}{NT_s},\ \ \frac{2\pi}{NT_s} \times 2,\ \ \frac{2\pi}{NT_s} \times 3,\ \ \cdots,\ \ \frac{2\pi}{NT_s} \times n,\ \ \cdots,\ \ \frac{2\pi}{NT_s} \times (N-1)$$

Or in general

$$X[n] = \sum_{k=0}^{N-1} x(k)\, e^{-j\frac{2\pi}{N}nk} \tag{2.62}$$

Equation (3.9) is the discrete Fourier transform of the discrete signal $x[k]$.

CHAPTER 3

Methodology and Data Analysis

3.1 Methodology

A new VHF (49.9 MHz) coherent back-scatter pulsed radar has recently become operational at the equatorial site Bahir Dar, Ethiopia ($11.6^0N, 37.3^0E$). The radar uses a 16 Kw transmitter operating in pulsed mode. The antenna system consists of a coaxial collinear array of 48 antennas. The beam from the antenna is tilted by 8^0 zenith angle towards east. The array is divided into two sections of eight antennas,each section being subdivided into four antenna pairs. The operating parameters of the radar are shown below in the table.

parameters	corresponding values
frequency	49.9 MHz
sample rate	200Hz
baud width	20 μ s
IPP	5 ms
samples per pulse	300

Since EEJ irregularities are field aligned,the radar's line of sight should be perpendicular to the

geomagnetic field lines to obtain strong and coherently scattered echoes. The inclination angle of the geomagnetic field at Bahir Dar is 8^0,hence to satisfy the above requirement, our BNR radar's line of sight is tilted by 8^0 from the vertical. The other important requirement to produce coherent back-scatter is that, the separation of field aligned irregularities (localized density structures) along the radar beam field must be equal to half of the radar wavelength (Bragg's condition) (Schlegel, 1973).

The very simplified diagram of BNR is shown in Fig (3.1) which includes some of the basic configuration requirements mentioned above. Thus from Bragg's condition, the relation between the wave vector of the transmitted radar signal ($\mathbf{k_t}$) and that of the the irregularity wave ($\mathbf{k_i}$) are related by

$$\mathbf{k_i} = -\mathbf{2k_t} \tag{3.1}$$

For a coherent radar operating at 49.9 MHz (our BNR radar is operating at this frequency) , equation (3.1) indicates that strong scattering of echoes will occur from an irregularity having wavelength of 3m. Radio signals from the radar should arrive coherently (a condition where two or more electromagnetic waves have phase difference which is equal to an integral multiple of 2π) at the field align irregularities so that the scattering from the irregularities is also coherent and as a result we will have strong echoes from the irregularities. Figure (3.2) shows sample radio signals (ray 1 and ray 2) from two sample antennas (antenna a and b) arriving coherently at the field aligned irregularities. As we discussed previously the angle between the rays and the geomagnetic field line is 90^0. Using the very known trigonometric formulas, the path difference

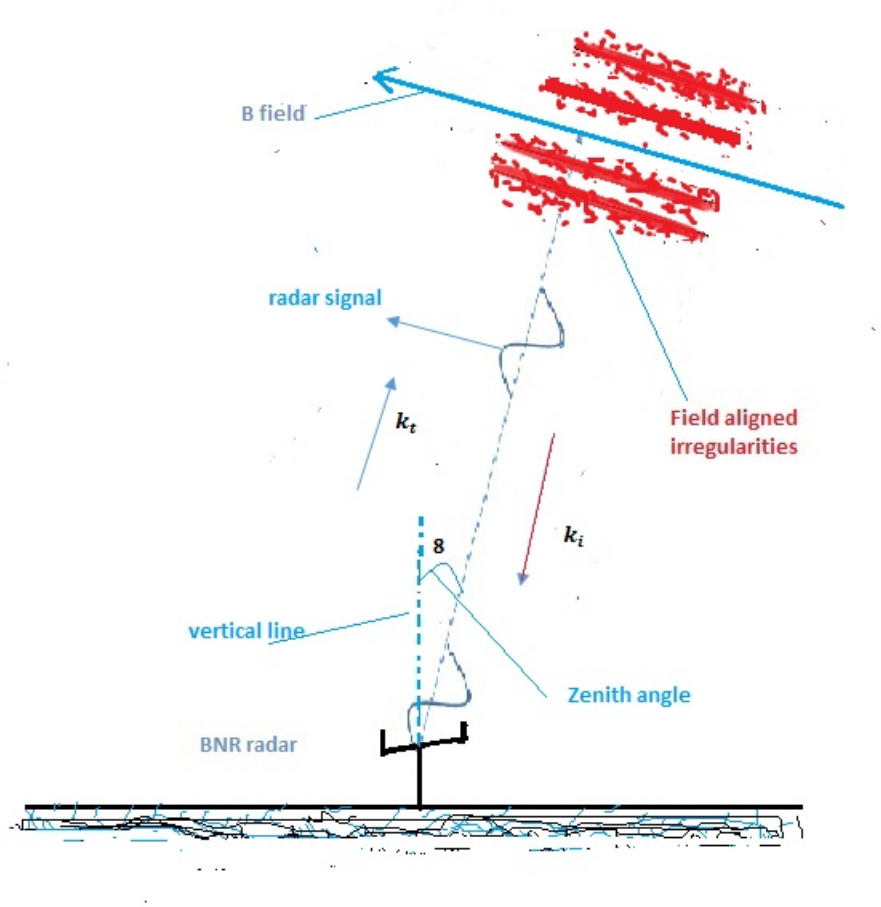

Figure 3.1: Schematic diagram of radar beam showing orthogonality to field-aligned irregularities and geometry of coherent radar observations.

between rays 1 and 2 is obtained to be

$$\Delta X = d \sin \theta.$$

where d is the distance between consecutive antenna systems whose magnitude in the case of BNR is equal to . Since lines 4 and 5 are parallel, the value of θ should be equal to the inclination angle of the geomagnetic field line over Bahir Dar region, i.e. $\theta = 8.33$. We know that the relation between path difference and phase difference is given by

$$\Delta\phi = \frac{2\pi}{\lambda}\Delta X.$$

Combining the above two equations gives the required values of phase difference between radio signals radiated from consecutive antenna systems to be

$$\Delta\phi = \frac{2\pi}{\lambda} d \sin \theta.$$

For coherent backscattering, $\Delta\phi = 2\pi$. Hence, the separation between the consecutive antennas becomes,

$$d = \frac{\lambda}{\sin \theta}$$

3.2 Data Analysis

The back-scattered echo received by the antenna array is amplified before passing through two phase-coherent detectors.In order to obtain a precise determination of the echo power spectrum,

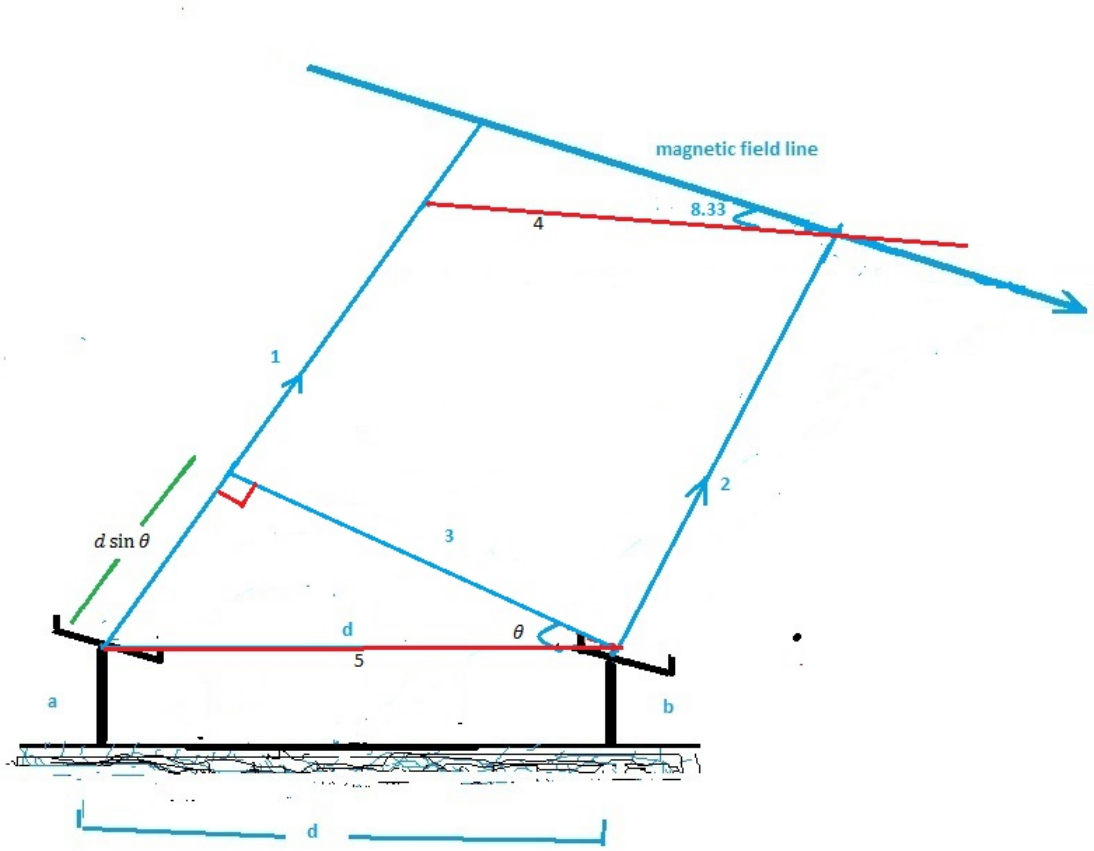

Figure 3.2: calculating phase difference between two radio signals radiated from two consecutive antenna systems

the signal returns from the electrojetir irregularities were coherently demodulated (i.e., the incoming signal was mixed with 'sine' and 'cosine' waves at the transmitted frequency and then filtered so that only the difference frequencies ere retained), preserving phase and amplitude information. The phase detected signals are sampled in 300 range bins (gates)which are separated by 0.75 km and stored in a sequential binary format. Therefore, 300 sample points will be taken for each transmitted pulse. Since the radar's inter-pulse pulse period is $5ms$, there should be 200 samples from each range bin in one second, that means the sampling rate or frequency,f_s is equal to 200 Hz. Samples of each pulse from each channel are integrated using the following formula.

$$\text{data}_{overall} = \frac{\sum_{c=1}^{8} c \times \text{data}_c}{8} \tag{3.2}$$

where c is channel number and data_c represents samples of the pulse from channel c. We used a matched filter technique to maximize signal to noise ratio. The Doppler spectra of the received echoes were obtained by FFT analysis that used 200-sample points for each range gate, thus resulting in one power spectrum per a second. Fifteen power spectra was calculated and averaged to produce a single power spectrum for every 15 seconds. Thus, for every 15 seconds we produced a single averaged Doppler power spectrum at each range gate. For every fifteen seconds,the total echo power from each range bins is then calculated by taking the sum of the Doppler power spectrum at that range gate. Hence,the 15 seconds average of the total spectral power was calculated as a function of height and local time, which is then presented as RTI maps.

The Doppler velocities of the irregularities were calculated using the Doppler shift formula for narrow band signal. For a narrowband signal propagating at the speed of light (c), the component of the phase velocity of the irregularity in the radar's line of sight was calculated by using the

known formula:

$$V = \frac{cf_d}{f_t} \tag{3.3}$$

where f_r is the frequency of the transmitted pulse, which is actually equal to 49.9MHz and the set of expected Doppler shifts,f_d were calculated as

$$f_d = -\frac{f_s}{2}, \cdots, -\frac{2f_s}{m-1}, -\frac{f_s}{m-1}, 0, \frac{f_s}{m-1}, \frac{2f_s}{m-1} \cdots, \frac{f_s}{2}$$

where, $m = 200$ is the number of sample points taken for FFT processing at every range bin and f_s is sampling frequency which is again equal to 200 Hz.

We have also used magnetometer data which was operational in 2015 at Addis Ababa, to produce the correlation graph between the strength of EEJ (which could be infrared from the daily variation of the horizontal component of the earth's magnetic field) and the strength of the returned echoes from its irregularities. Since there is no magnetometer which is at a nearby distance to Addis Ababa but outside of the latitudinal extent of EEJ, we couldn't remove the effect of other space currents. The background horizontal component of earth's magnetic field is removed by subtracting the night time value of the earth's magnetic field.

CHAPTER 4

Results and Discussions

Range time intensity (RTI) map of radar echoes scattered from equatorial electrojet irregularities observed by the Blue Nile Radar (BNR) in the year of 2015 on selected days with strong echoes are presented in this thesis work. The most probable occurrence height of EEJ irregularities are also determined for each seasons. The local time variation of total echo power for each season is also discussed in this work. Finally and more importantly, the power spectra of the irregularities observed on October 15, 2015 and March 25,2.07 is discussed and analyzed in detail. Due to the automatic deletion of the binary data there is lack of enough binary data type to produce power spectral plots in a single year. Therefore, instead of relying on a single year data like the RTI maps ,we used all accessible binary data files irrespective of the year it is obtained.

4.1 Results and Interpretations

Figure 4.1 shows the range-time-intensity (RTI) map of the returned echos for selected days. The range and time resolutions of the RTI maps are 0.75 km and 15 seconds respectively.

A close examination of the RTI maps of all figures reveals neither a significant descent nor ascent of the EEJ scattering region during both before and post noon hours (the scattering region is

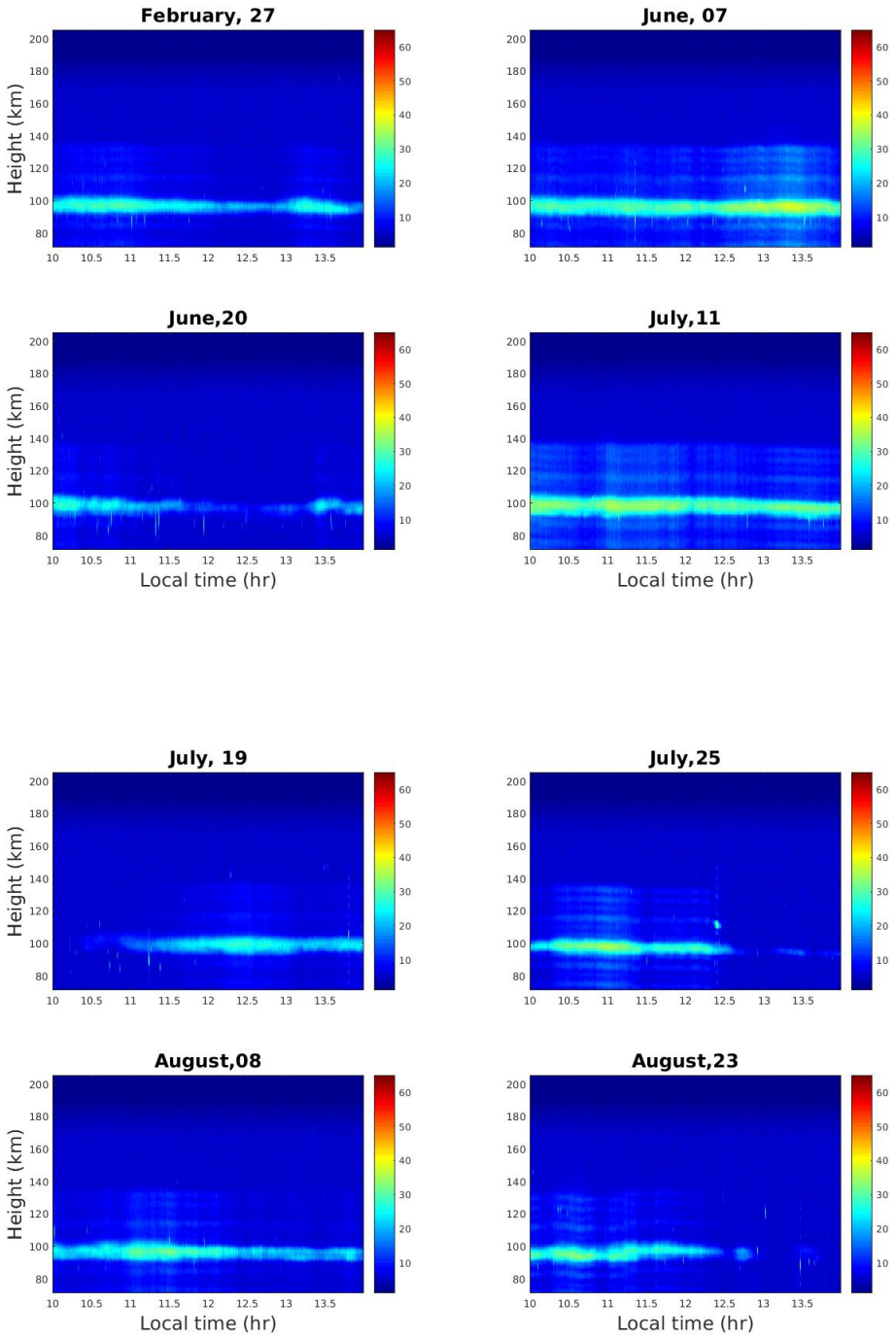

Figure 4.1: RTI maps of selected quit days in 2015

almost stratified horizontally). But at other longitudinal sectors, such as at Sao Luis (Abdu *et al.*, 2002) and at Gadanki, India (Patra *et al.*, 2004) , it has been reported that there was regular descent and rise in the EEJ scattering region during the pre and post-noon hours respectively. A close inspection of all RTI maps can give an insight that the height of the peak power in the RTI maps seems to be centered around 99-102 km with some day-to-day variations. Although we expect a peak echo power near the midday (the time at which maximum electrojet intensity is registered as can be inferred from local time variation of the H-component of the magnetic field), the RTI maps shows that there is no systematic tendency in these sets of days for a local time preference for the occurrence of a daytime peak power. Strong radar echoes were observed throughout the daytime operational hours of the radar (10 LT -14 LT) during February 27, June 07 and July 11.

The correlation between the strength of the day time horizontal component of earth's magnetic field contributed by the EEJ (assuming that the effect of other ionospheric currents is negligible) and the strength of the averaged echo from the corresponding irregularity for February 27, August 08 and 23 is also presented in Fig (4.2). The background magnetic field is removed by subtracting the value of the earth's magnetic field recorded during the night time. Unfortunately, there was no magnetometer data for the entire months of June and July to produce the same correlation plot for the other days whose RTI map is presented in Fig. (4.1). From the plots in Fig (4.2) one can see simply that, very good correlation is observed before noon hours than after noon hours for August 08 and February 27 while for August 23 the correlation extends after noon time hours. From Fig (4.1) one can see that, the intensity of the radar echo for August 23 is very strong

during both before and after noon time hours while for that of August 08 and February 27, the strength of the echo decreases during post noon time hours. Similar fashion is observed on the aspect of the correlation between the strength of EEJ and echo of its irregularities. This indicates that to observe very good correlation between the two parameters, the intensity of echoes from the EEJ irregularities should exceed some threshold value and there is daily variation in the value of this threshold intensity. Further analysis and investigation will be given in another work regarding the dependence of the correlation on the threshold value. In addition, we will use two magnetometers, one in the zone of EEJ and the other outside of EEJ, to examine if the effect of other space currents is the reason for observed poor correlations. Cohen & Bowles (1963) have also reported very good correlation between the strength of the echoes received from EEJ irregularities and the current density in the electrojet.

The most probable height of EEJ irregularities, from which maximum echoes are received, for each season of the year 2015 is presented in Figs. (4.3) and (4.4). The height of the peak echo power for every 15 seconds is first evaluated from the RTI map and then averaged over one day. Thus, the average height of the peak echo is evaluated for each day of the season. All of the bar plots in Figs (4.3) and (4.2) indicate that,for all seasons of the year, the most frequent height of occurrence of EEJ irregularities is between 99 and 102 km. The reason for the occurrence of EEJ irregularities most frequently about this height is certainly connected to the value of polarization electric field, which is actually the driving force of the irregularities in EEJ. Since $\frac{\sigma_H}{\sigma_P}$ is maximum around 100km (Fig (2.5)), the driving vertical electric field $E_z = \frac{\sigma_H}{\sigma_P} E_y$ should also be maximum there. In addition to this, the gradient of electron number density is also strong and upward about

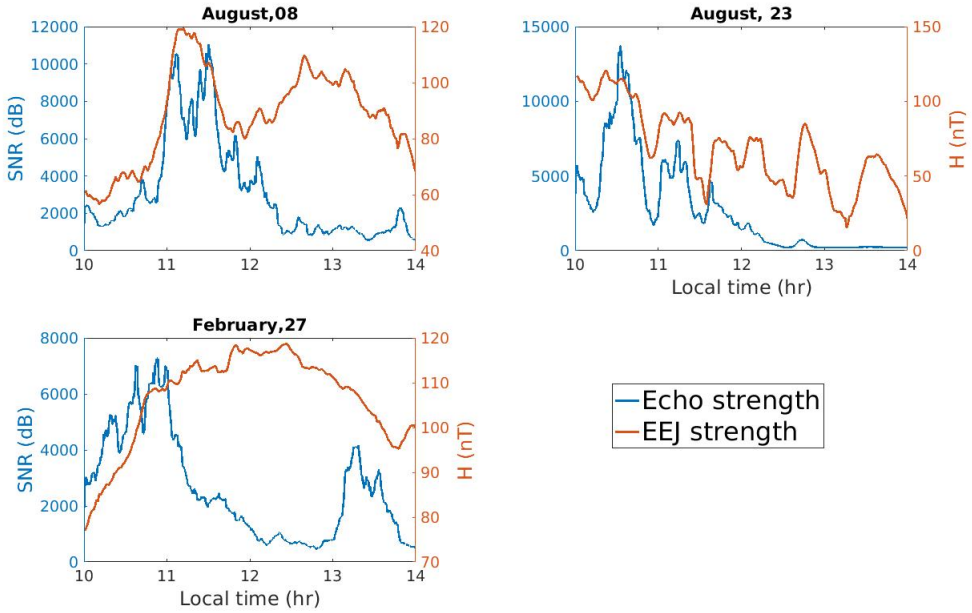

Figure 4.2: Correlation between strengths of echos from EEJ irregularities and EEJ's magnetic field

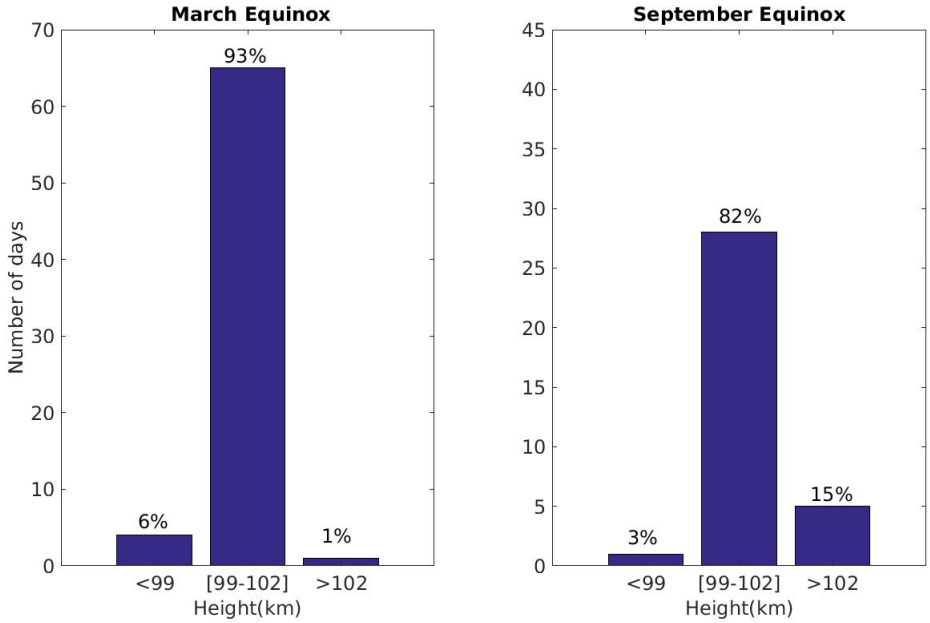

Figure 4.3: Most probable height of EEJ irregularities for equinoctial months in the year 2015

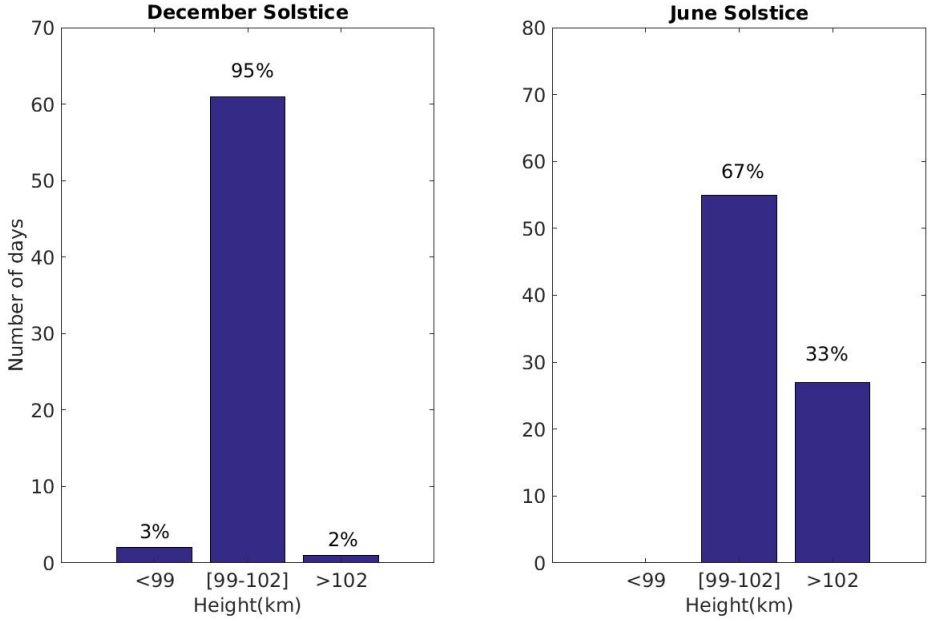

Figure 4.4: Most probable height of EEJ irregularities for solstice months in the year 2015

the region of 100 km (Fig (2.1)). These two conditions are the favorable requirements for the generation of gradient drift instability and hence type II irregularities about the height of 100 km. Patra *et al.* (2004) over the region of Gadanki, India has also found that the most frequent echoing region of EEJ was between 95 and 100 km. This person has also observed rise in the height of the most probable echoing region during summer (which shares many months with June solstice). Similarly, we found that during June solstice (Fig 4.4) there is an increase in the number of days whose corresponding echoes were coming from a region of height greater than 102 km. This may be due to the fact that during summer season (june solstice) the earth's atmosphere gets lower amount of solar radiation and as a result the bottom part of E region (about a height of 100 km) vanishes. This will results in the rise of the electrojet and correspondingly its irregularity to a higher region where the Cowling conductivity becomes maximum. That means, due to lack of enough electron number density, the ionospheric conductivities there in general and specifically the Cowling conductivity (which is the driving force of electrojet) will be minimum (because electron number density and conductivity are related positively). Thus, the electrojet as a result is forced to move upward where enough charge carriers are found and as a result its irregularities will also move upward during June solstice.

Diurnal (Local time) variation of the the most probable height of EEJ irregularities for each season is also produced and presented in Fig. (4.5). The value of this height varies with local time but the variation is confined in the interval of 99 - 100 km which is in agreement with the bar plots in Figs.(4.3) and (4.4). On average, throughout the whole day time hours (actually between 10:00 LT and 14:00 LT in which the radar is operational) the height of the peak echoes in June solstice is

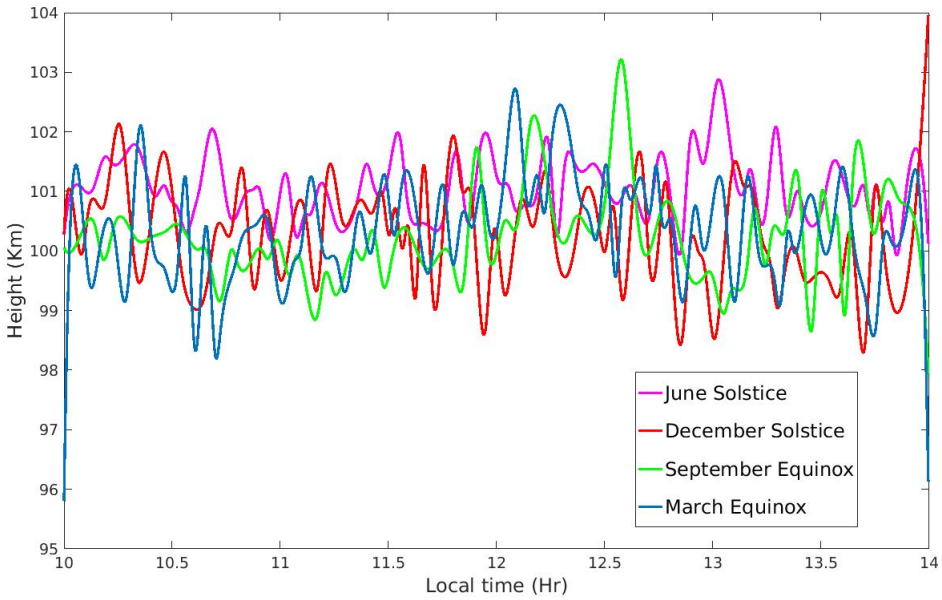

Figure 4.5: Local time variation of most probable height of EEJ irregularities for each season in the year 2015

greater than that of other seasons and this is also in agreement with the bar plots presented in Fig (4.4). In addition, the plots in Fig. (4.5) directly reveals that the height of the peak power increase and then immediately decrease with local time in a random fashion. Local time variation of the total echo power from the scattering regions for each season is also produced and depicted in Fig. (4.6). The plots are produced by taking the sum of the echo power coming from regions which are between the lowest (87 km) and the highest (130km) possible height of EEJ irregularities at every 15 seconds from the RTI map for each day of the season and then averaged over the total number of the days in the season considered. A close examination of the plots can indicate the most frequent local time for the occurrence of EEJ irregularities. From the graphs, for all seasons

it can be seen that the highest echo of EEJ irregularities are occurred before and after the noon time except some strong echoes at noon time which cover very short period of time which is less than 30 minutes. The same local time statistical occurrence of EEJ irregularities has also been observed by Baiqi1 *et al.* (2012) at Hainan, China and Patra *et al.* (2004) at Gadanki, India. Patra *et al.* (2004) reported that the most probable times for echoes were found to be just after sunrise (95%), just before sunset (80%), and least likely around noon 30%. Absence of strong echo during noon time is also clearly observed in the RTI maps shown in Fig. (4.1). The absence of noon time echoes was found to be due the movement of the dip equator (Sekar *et al.*, 2013). The researchers conducted a systematic ground based magnetometer measurements at THumba ($8.73^0 N, 77.8^0$ E), which has similar latitudinal position to our observation sight, Bahir dar. The study found that the streaming plasma waves (irregularities) over Thumba during magnetically quit periods exist when the dip angle is less than 1.5^0 and these waves were generally absent whenever the dip angle is greater than or equal to 1.5^0. That means whenever the dip angle of the observed region is greater than 1.5^0, the probability that this region being outside of the latitudinal extent of EEJ will be high. Since dip angle of our observation site,Bahir Dar, is greater than 1.5^0, the absence of the echoing regions during noon time may be connected to the movement of the dip angle as those observed in Thumba, India. Throughout the whole local time of the days, irregularities observed during March equinox were more intense than those observed at other seasons as shown in Fig. (4.6). The same seasonal variation of scattered echo power was also observed by Chau1 *et al.* (2002) at Piura. Similarly, the strength of the equatorial electrojet was also found to be maximum during equinoctial months (Venkatesh1 & Prasad, 2015). Therefore,

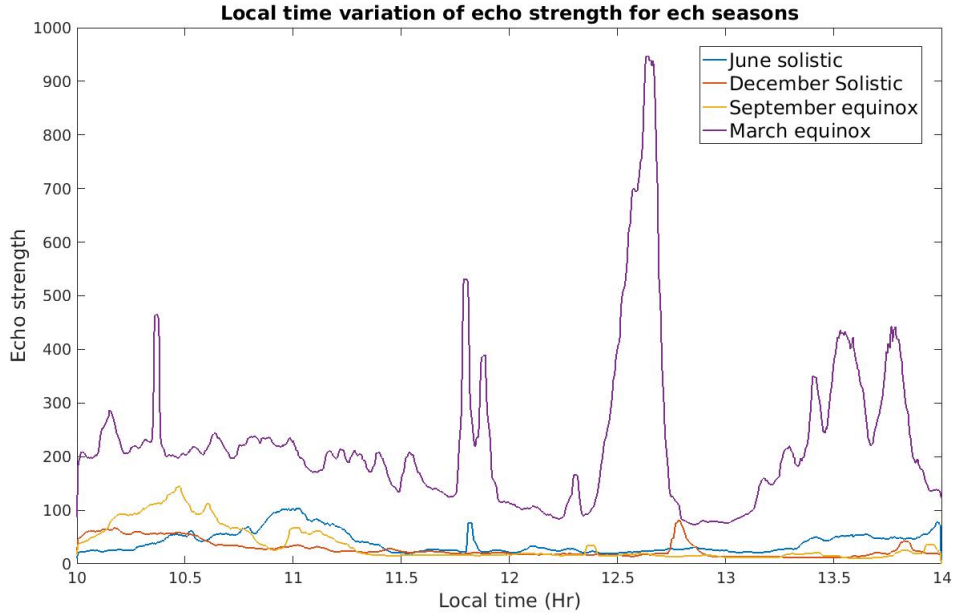

Figure 4.6: Diurnal variation of echo strength for each seasons of the year 2015

observing strong irregularities (echoing regions) during March equinox should certainly related to the increment of the corresponding electrojet strength. In principle, whenever the velocities of the streaming electrons in EEJ increase, the strength of EEJ will also increases. Now if the velocity of the electrons exceeds some threshold value (actually this threshold value should be equal to ion acoustic velocity), two stream instability will grow and hence EEJ irregularities will be generated. On the basis of physical mechanisms, during equinoctial months the equatorial region of the ionosphere is overhead to the sun and as a result the strong solar radiation gives rise to strong horizontal electric field and more importantly strong polarization electric field which is the driving force of EEJ irregularities.

The power spectra associated with an irregularity observed on October 15,2015 and March 25,

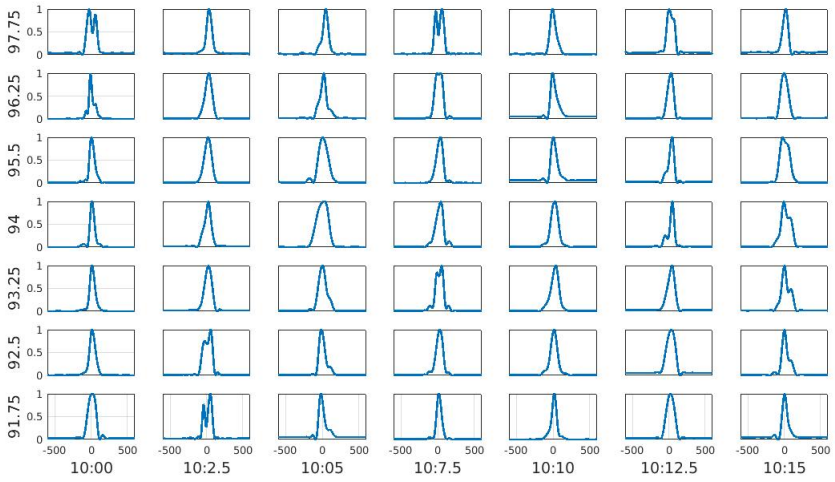

Figure 4.7: Power spectra of the irregularities observed on October 15,2015

2017 as a function of height bins and local time are presented in Fig (4.7) and Fig (4.8). The vertical labels are heights in kilometers while the horizontal labels are local times in hours. The discussion will mainly concentrate on the power spectral of March 25,2017 because, except on the magnitude of Doppler shifts, there is no any difference between the spectral plots of the two days. The spectra are all normalized to a peak value of unity, and thus the areas under the curves are not proportional to the signal power. That means except the phase velocity of the irregularities, we can't infer any other parameter from the spectral plots. The spectrogram is produced corresponding to a local time and height interval of more intense radar echoes i.e. between 11 LT and 11.5 LT and 93.25 and 102.25 km for the irregularity observed on March 25 . Sample power spectra are produced with an interval of 5 minutes at each selected height bins.

As we described in the methodology part, each power spectrum in the figure below consists of 15 power spectra averaged over 15 seconds. Where, each of these spectra (that is, the basic

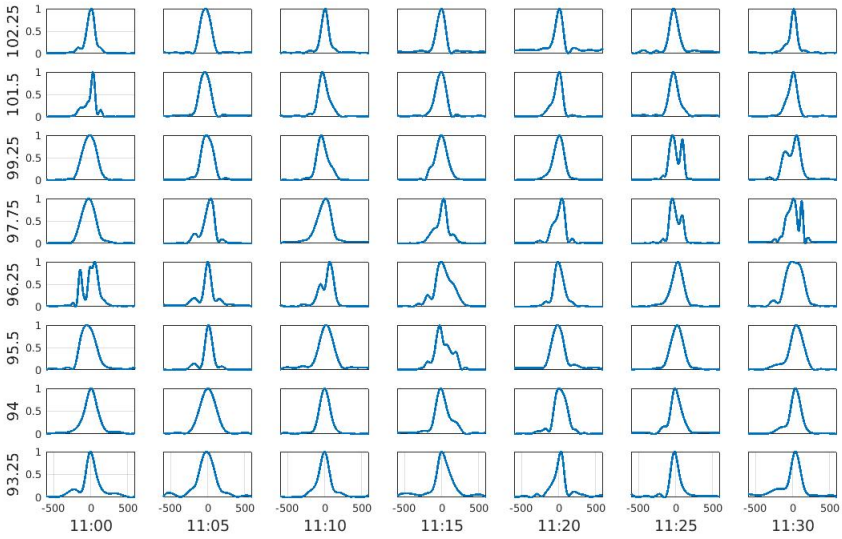

Figure 4.8: Power spectra of the irregularities observed on March 25,2017

individual spectrum) was calculated at 1-s intervals at each range gate. The power spectra plots are produced by plotting the power of the returned echo (but normalized) against the Doppler velocity as described in the methodology part in detail.

Except at some range bins, the peak of the power spectra are centered at zero or very small Doppler shifts. Relatively none zero but very small Doppler shifts are also observed, for example, at 11:00 LT and 11 :30 LT correspondingly at a height of 95.5 km. The Doppler shift at local time of 11:00 is negative with an equivalent phase velocity of -51.36m/s and that of 11:30 is positive with an equivalent phase velocity of 63.44m/s. Positive Doppler shifts are observed for an irregularity moving towards the radar (almost vertically downward, since our BNR radar is pointing almost vertically upward) and negative Doppler shifts are observed for an irregularity moving away from the radar (vertically upward). Power spectra with double peaks are also

observed for example at a height of 96.25 and a local time of 11:00. This result is in agreement with other findings in another longitudinal sectors (Kudeki *et al.*, 1987). physically , the ,peaks represent irregularity waves traveling upwards and downwards at that region. That means, at the given instant of time and height but at different horizontal positions, there are two different irregularities traveling upwards and downwards. Another group of researchers suggests that such double peaks represents a composite spectrum of type I and type II as observed by the 50 MHz radar at Sao Luis, Brazil (Abdu *et al.*, 2002)

Irregularities with zero or very small (actually it should be less than the ion acoustic velocity in the order of 350 m/s) Doppler shift power spectra are categorized under type II irregularity waves. These irregularities are believed to be generated by gradient drift instability (Balsley, 1969). The basic reason that we couldn't observe irregularities whose corresponding power spectra attain peaks at greater Doppler shifts relies on equations (2.56) and (2.58). According to these equations if the radar's line of sight ($\mathbf{k_t}$) is perpendicular to the drift direction of electrons ($\mathbf{V_d}$), the phase velocity of the irregularity will becomes zero.

Previous researchers have found that (Balsley, 1969), electrons in the electrojet are found to drift horizontally from east to west in the daytime. Thus, since our radar's line of sight ($\mathbf{k_t}$) is almost vertical and the drift velocity of electrons ($\mathbf{V_d}$) is horizontal , the phase velocity of the irregularities should be zero according to the equations given in (2.56). On the other hand, equation (2.58) indicates that greater Doppler shift will occur when the echo is returned from an irregularity wave which is traveling towards the radar (vertically downward) or away from the radar(vertically upwards). This has been also verified by an other researcher (Balsley, 1969).

In his experiment at the Jicamarca radio observatory, Balsely has probed the EEJ irregularities nearly at the same time by using an oblique and vertical radars. In the result, Balsley (1969) found that when the radar's line of sight is vertical the peak of the power spectrum occurs at zero Doppler shift and when the radar's line of sight is tilted either towards the west or east the power spectrum attains its peak to greater Doppler shift (Fig.(2.8)). In general, based on the basic principles displayed in equation (2.56) and (2.58) we can conclude that there were no irregularities (except at some heights) moving up and down in our observational sector of EEJ. There was also another observation with a result of type II irregularities for all time and altitudes at Gadanki by Patra *et al.* (2004). The researcher used a radar tilted from vertical by 13.2^0 which is approximately similar to our radar's tilt angle. There fore, we can say that our observation is in agreement with the basic physical equations and previous observations.

CHAPTER 5

Conclusions and Recommendations

In this thesis radar echoes of equatorial electrojet irregularities have been obtained from Blue Nile coherent backscatter radar, which is deployed at Bahir Dar,Ethiopia. The echo have been analyzed to investigate the characteristics of EEJ irregularities. The following concluding remarks are drawn using the analyzed radar echoes

5.1 Conclusion

In our observation, it is found that EEJ irregularities occur frequently between 99 and 102 km. Relative to other seasons, echoes were received from a height greater than 102 km for many number of days during June solstice. Strong irregularities have occurred during March equinox than other seasons. Irregularities with type II radar echo were observed for most of the local hours and heights. Irregularities having double peak power spectra were also observed at some instants of times and heights over Bahir Dar sector of EEJ. This shows that most of the time the EEJ irregularities in our sector are driven by the gradient drift instabilities.

5.2 Recommendation

Since the BNR radar at this time is out of operation, we strongly recommend that it should be make to be operational very soon. In addition, the day time operational hours of the radar is between 10 LT and 14 LT which is very short. So, in the future it should be upgraded so that it can work at least for 8 hours which enables us to observe a full diurnal variation of EEJ irregularity intensities. In addition the radar should be upgraded so that it can be tilted at different zenith angles and this could enable us to scan in the East - West plane of the EEJ region.

Our future work will concentrate on investigating the equatorial electrojet at oblique zenith angle so that we can examine if there are type I irregularities in addition to type II. The contribution of wind for the occurrence EEJ irregularities over Bahir Dar should be considered in the future works.

References

ABDU, A., DENARDINI, C. & SOBRAL, A. (2002). Equatorial electrojet irregularities investigations using a 50 mhz back-scatter radar and a digisonde at sao luis: some initial results. *Journal of Atmospheric and Solar-Terrestrial Physics*, **64**, 14251434.

BAIQI1, N., LIANHUAN1, H., GUOZHU1, L. & LIBOL, L. (2012). The first time observations of low-latitude ionospheric irregularities by vhf radar in hainan. *Journal of Atmospheric and Solar-Terrestrial Physics*, **55**, 11891197.

BALSELY, B. (1973). Radar observations of two-dimensional turbulence in the equatoriael lectroiet. *Journal of Geophysical Research*, **78**.

BALSELY, B. & FARLEY, T. (1971). Radar studies of equatorial electrojet at three frequencies. *Journal of Geophysical Research*, **76**.

BALSLEY, B. (1969). Some characteristic5 of non-two-stream irregularities in the equatorial electrojet. *Journal of Geophysical Research*, **74**.

BURROWS, K. (1970). The day-to-day variability of the equatorial electrojet in peru. *Journal of Geophysical Research*, **75**.

CAHIL, L. (1959). Investigation of the equatorial electrojet by rocket magnetomete. *Journal of Geophysical Research*, **64**.

CARTER, D., BALSLE, B. & ECKLUND, W. (1976). Vhf doppler radar observations of the african equatoriale lectrojet. *Journal of Geophysical Research*, **81**.

CHAPMAN, S. (1951). Some phenomena of the upper atmosphere. *Proc. Phys. Soc. London*, **64**, 833–844.

CHAU1, J., WOODMAN, R. & FLORES, L. (2002). Statistical characteristics of low-latitude ionospheric field-aligned irregularities obtained with the piura vhf radar. *European Geophysical Society*, **20**, 12031212.

COHEN, B. & BOWLES, B. (1967). Secondary irregularities in the equatorial electrojet. *Journal of Geophysical Research*, **72**.

COHEN, R. & BOWLES, K. (1963). The association of plane-wave electron-density irregularities with the equatorial electrojet. *Journal of Geophysical Research*, **68**.

COHN, R. (1973). Phas ve elocities of irregularitieins in the equatorial electrojet. *Journal of Geophysical Research*, **78**.

FARLEY, T. (1963a). A plasma instability resulting in field aligned irregularities in the ionosphere. *Journal of Geophysical Research*, **68**, 60836097.

FARLEY, T. (1963b). A plasma instability resulting in field-aligned irregularities in the ionosphere. *Journal of Geophysical Research*.

FARLEY, T. (1973). Instabilitieis in the equatorial electroiet. *Journal of Geophysical Research*, **78**.

FARLEY, T. (1985). Theory of equatorial electrojet plasma waves:newdevelopments and curren tstatus. *Journal of Atmospheric and Solar-Terrestrial Physics*, **42**, 729.

FEJER, G. & KELLEY, M. (1980). Ionospheric plasma irregularities. *Rev.Geophys*, **18**, 401–454.

HEI, M.A., HEELIS, R.A. & MCCLURE, J. (2005). Seasonal and longitudinal variation of large scale topside equatorial plasma depletions,. *Journal of Geophysical Research*, **110**.

KELLEY, M. (1989). The earths ionosphere. *International Geophysics Series*, **43**.

KELLEY, M., CUEVAS, R. & HYSELL, D. (2008). Radar scatter from equatorial electrojet waves: An explanation for the constancy of the type i doppler shift with zenith angle. *Geophysical research letter*, **35**.

KUDEKI, E., FEJER, G., FARLEY, T. & HANUISE, C. (1987). The condor equatorial electrojet campaign:radar results. *Journal of Geophysical Research*, **92**, 1356113577.

MANGISTU, E. & KASSA, T. (2015). Temporal characteristics of the equatorial electrojet and counter electrojet over ethiopian sector. *Advances in Space Research*, **55**, 566–575.

MURALIKRISHNA, S. (1976). The nature of electric field in the e region close to morning and evening reversals. *Geophysical Research Letter*, **8**.

NIGUSSIE, M. (2014). *Modeling The East African Ionosphere*. Ph.D. thesis, Washera Geospace and Radar Science Research Laboratory, Departement of Physics, Bahir Dar University.

OSBORNE, G. (1963). Daily and seasonal changes of the equatorial electrojet in peru. *Journal of Atmospheric and Terrestrial Physics*, **26**, 1097–1105.

PATRA, A. (2005). East west asymmetries of the equatorial electrojet 8.3 m type-2 echoes observed over trivandrum and a possibl eexplanation. *Journal of Geophysical Research*, **101**.

PATRA, A., SRIPATHI, S., SIVAKUMAR, V. & RAO, P. (2004). Statistical characteristics of vhf radar observations of low latitude e-region field-aligned irregularities over gadanki. *Journal of Atmospheric and Solar-Terrestrial Physics*, **66**, 16151626.

RAGHAVARAO, R. (2002). Equatorial e region irregularities:a review of recent observations. *Journal of Atmospheric and Solar-Terrestrial Physics*, **64**, 1435–1443.

RAGHAVARAO, R. & DAGAR, R. (1982). Dynamo region and the equatorial electrojet in the jovian atmosphere. *planetary Space science*, **31**, 633–640.

SCHLEGEL, K. (1973). Coherent backscatter from ionospheric e-region plasma irregularities. *Journal of Atmospheric and Solar-Terrestrial Physics*, **58**, 933–941.

SEBA, E. & NIGUSSIE, M. (2016). Investigating the effect of geomagnetic storm and equatorial electrojet on equatorial ionospheric irregularity over east african sector. *Advances in Space Research*, **58**, 1708–1719.

SEKAR, R., GUPTA, S., ACHARYA, Y., CHAKRABARTY, D., PALLAMRAJU, D., PATHAN, B., TIWARI, D. & CHOUDHARY, R. (2013). Absence of streaming plasma waves around noon time over thumba in recent times:isitrelated to the movement of the dip equator? *Journal of Atmospheric and Solar-Terrestrial Physics*, **103**, 8 –15.

SUDAN, N., AXINRMISI, J. & FARLEY, T. (1973). Generatioonf small-scale irregularities in the equatorial electrojet. *Journal of Geophysical Research*, **78**.

VENKATESH1, K. & PRASAD, P.F.D. (2015). Day-to-day variability of equatorial electrojet and its role on the day-to-day characteristics of the equatorial ionization anomaly over the indian and brazilian sectors. *Journal of Geophysical Research*, **20**, 12031212.